

# Constitutive Modeling of Brain Tissue: Current Perspectives

*Modeling the mechanical response of the brain has become increasingly important over the past decades. Although mechanical stimuli to the brain are small under physiological conditions, mechanics plays a significant role under pathological conditions including brain development, brain injury, and brain surgery. Well calibrated and validated constitutive models for brain tissue are essential to accurately simulate these phenomena. A variety of constitutive models have been proposed over the past three decades, but no general consensus on these models exists. Here, we provide a comprehensive and structured overview of state-of-the-art modeling of the brain tissue. We categorize the different features of existing models into time-independent, time-dependent, and history-dependent contributions. To model the time-independent, elastic behavior of the brain tissue, most existing models adopt a hyperelastic approach. To model the time-dependent response, most models either use a convolution integral approach or a multiplicative decomposition of the deformation gradient. We evaluate existing constitutive models by their physical motivation and their practical relevance. Our comparison suggests that the classical Ogden model is a well-suited phenomenological model to characterize the time-independent behavior of the brain tissue. However, no consensus exists for mechanistic, physics-based models, neither for the time-independent nor for the time-dependent response. We anticipate that this review will provide useful guidelines for selecting the appropriate constitutive model for a specific application and for refining, calibrating, and validating future models that will help us to better understand the mechanical behavior of the human brain. [DOI: 10.1115/1.4032436]*

**Rijk de Rooij**

Department of Mechanical Engineering,  
Stanford University,  
Stanford, CA 94305  
e-mail: rderooij@stanford.edu

**Ellen Kuhl<sup>1</sup>**

Department of Mechanical Engineering,  
Stanford University,  
Stanford, CA 94305  
e-mail: ekuhl@stanford.edu

## 1 Introduction

The importance of understanding the mechanical properties of the brain tissue has been acknowledged for over half a century [1]. It was first suggested, and confirmed, that severe rotations of the skull induce shear strains, which may lead to concussion or brain injury [2]. Shortly after, the need to understand the mechanical response of the brain tissue was recognized. In addition to gaining insight into brain injury, the mechanical properties of the brain were also suggested to be relevant for developing surgical tools and procedures, and, more recently, for understanding neurodevelopment and drug and oxygen transport in the brain [3].

With an elastic modulus of only 1 kPa, the brain tissue is among the softest of all mammalian tissues [4]. The absence of mechanical forces in its physiological environment is generally offered as an explanation. Despite a large variation in the reported material parameters values—even in parameters as simple as the material stiffness—several characteristics of the brain tissue response are now well established [5]: There is a general agreement that the elastic response of the brain tissue is highly nonlinear; in fact, its linear strain limit has been reported as low as 0.1% [6]. In addition, experiments have consistently shown that the brain tissue is viscoelastic, its response is highly sensitive to the loading rate, and displays the characteristic phenomena associated with relaxation and creep [7].

A constitutive model for the brain tissue has to explain the experimental data with one or more material parameters. Every material parameter that has been reported in the literature is, either explicitly or implicitly, related to the choice of the constitutive model. Over the past decades, with the advancement of numerical modeling, it has become increasingly common to formulate constitutive models for soft biological tissues within the general setting of finite deformation continuum mechanics [8]. This is often in sharp contrast with experimental techniques, which are typically based on a linear approach with simple, homogeneous one- or two-dimensional load cases [9]. This discrepancy of theory and

experiment puts additional constraints on the selection of constitutive models and the identification of model parameters.

Here, we review the most popular state-of-the-art models for the brain tissue, which have been proposed in the literature. Typically, these models can be divided into multiple building blocks, each describing a specific aspect of the material response: time-independent, time-dependent, or history-dependent [10]. We categorize these different aspects in a structured manner, which allows us to identify commonalities and to highlight differences among the individual models. Within each building block, we attempt to cover the range from relatively simple, phenomenological toward more complex, mechanistic models [11]. Our main objective is to provide guidelines for selecting an appropriate constitutive model based on the physical motivation and practical relevance for a specific, particular application.

We begin by briefly summarizing the governing equations of continuum kinematics and finite hyperelasticity in Secs. 2 and 3. These sections are not specific to the brain tissue, but they contain concepts that are widely used in the brain tissue modeling today. We then focus specifically on the time-independent, hyperelastic modeling of the brain tissue in Sec. 4. Subsequently, we provide an overview of the time-dependent modeling of brain tissue, which includes viscous, porous, and electromechanical effects in Sec. 5. Experimental evidence suggests that the mechanical response of the brain tissue is also affected by the loading history, which motivates the discussion of the history-dependent modeling of the brain tissue in Sec. 6. We close by discussing the different constitutive models for brain tissue in Sec. 7. The discussion is guided by an overview of the constitutive models in tabular format. We evaluate current models based on their physical motivation and practical relevance, provide guidelines for selecting a model, and point out open challenges, perspectives, and directions for future research.

## 2 Kinematics

In this review, we model the brain at the macroscopic scale and adopt a continuum approach. On this scale, constitutive models for brain tissue relate tissue deformations to tissue stresses. In this

<sup>1</sup>Corresponding author.

Manuscript received September 1, 2015; final manuscript received December 29, 2015; published online January 18, 2016. Editor: Harry Dankowicz.

section, we briefly summarize the general framework of finite deformation continuum kinematics that is relevant to brain tissue.

**2.1 Continuum Kinematics.** We consider a body that occupies a region  $\mathcal{B} \in \mathbb{R}^3$  in its undeformed, stress-free configuration. A motion  $\boldsymbol{\varphi}$  maps every point  $\mathbf{X} \in \mathcal{B}$  to another point  $\mathbf{x} \in \mathbb{R}^3$  in space. This motion is generally time-dependent and thus  $\boldsymbol{\varphi}(\mathbf{X}, t) : \mathcal{B} \times \mathbb{R}_+ \mapsto \mathbb{R}^3$ . For biological tissues including the brain, it is difficult to uniquely identify an undeformed, stress-free reference configuration since many soft tissues are prestressed in their physiological state [12,13]. In practice, most approaches choose the physiological prestressed configuration as reference configuration. Strains, and thereby stresses, are not directly related to the deformation mapping  $\boldsymbol{\varphi}$ , but rather to the deformation gradient  $\mathbf{F}$ . The deformation gradient, the spatial derivative of the deformation map  $\boldsymbol{\varphi}(\mathbf{X}, t)$  at fixed time  $t$ , characterizes the relative deformation through the mapping between line elements

$$\mathbf{F} = \frac{d\boldsymbol{\varphi}}{d\mathbf{X}} = \nabla_{\mathbf{X}}\boldsymbol{\varphi} \quad (1)$$

The deformation gradient introduces the left and right Cauchy-Green deformation tensors  $\mathbf{b}$  and  $\mathbf{C}$  as characteristic deformation measures

$$\mathbf{b} = \mathbf{F} \cdot \mathbf{F}^T \quad \text{and} \quad \mathbf{C} = \mathbf{F}^T \cdot \mathbf{F} \quad (2)$$

The right Cauchy-Green deformation tensor defines the Green-Lagrange strain tensor, a strain measure associated with the reference configuration

$$\mathbf{E} = \frac{1}{2}[\mathbf{C} - \mathbf{I}] \quad (3)$$

To ensure objectivity, constitutive models are generally a direct function of the deformation tensors  $\mathbf{b}$  or  $\mathbf{C}$ , or rather of their invariants,  $I_1, I_2$ , and  $I_3$

$$\begin{aligned} I_1 &= \text{tr}(\mathbf{b}) = \text{tr}(\mathbf{C}) \\ I_2 &= \frac{1}{2}[\text{tr}^2(\mathbf{b}) - \text{tr}(\mathbf{b}^2)] = \frac{1}{2}[\text{tr}^2(\mathbf{C}) - \text{tr}(\mathbf{C}^2)] \\ J^2 &= I_3 = \det(\mathbf{b}) = \det(\mathbf{C}) \end{aligned} \quad (4)$$

in which  $J = \det(\mathbf{F})$  represents the change in volume between the reference and current configurations. By definition, these invariants are independent of coordinate transformations. Their partial derivatives with respect to the left and right Cauchy-Green deformation tensors will be useful to relate relative deformations to stresses

$$\frac{\partial I_1}{\partial \mathbf{C}} = \mathbf{I}, \quad \frac{\partial I_2}{\partial \mathbf{C}} = I_1 \mathbf{I} - \mathbf{C}, \quad \text{and} \quad \frac{\partial I_3}{\partial \mathbf{C}} = J^2 \mathbf{C}^{-1} \quad (5)$$

Constitutive models often consider the volume preserving, or isochoric, contribution to the deformation separately. This part of the deformation can be isolated with the isochoric left and right Cauchy-Green deformation tensors,  $\bar{\mathbf{b}}$  and  $\bar{\mathbf{C}}$

$$\bar{\mathbf{b}} = J^{-2/3} \mathbf{b} \quad \text{and} \quad \bar{\mathbf{C}} = J^{-2/3} \mathbf{C} \quad (6)$$

such that the isochoric invariants become

$$\bar{I}_1 = J^{-2/3} I_1, \quad \bar{I}_2 = J^{-4/3} I_2, \quad \text{and} \quad \bar{I}_3 = 1 \quad (7)$$

The temporal derivative of  $\boldsymbol{\varphi}(\mathbf{X}, t)$  at fixed position  $\mathbf{X}$  represents the velocity  $\mathbf{v}(\mathbf{X}, t)$

$$\mathbf{v} = \frac{d\boldsymbol{\varphi}}{dt} = \dot{\boldsymbol{\varphi}} \quad (8)$$

Similar to the deformation gradient  $\mathbf{F}$ , which relates strains to stresses, the spatial velocity gradient  $\mathbf{l}$  relates strain rates to stress rates. The velocity gradient  $\mathbf{l}$  is the spatial gradient of the velocity field  $\mathbf{v}$

$$\mathbf{l} = \frac{\partial \mathbf{v}}{\partial \mathbf{x}} = \nabla_{\mathbf{x}} \mathbf{v} = \dot{\mathbf{F}} \cdot \mathbf{F}^{-1} = \mathbf{d} + \mathbf{w} \quad (9)$$

The spatial velocity gradient is often decomposed into its symmetric and skew-symmetric parts, which represent the stretch rate  $\mathbf{d}$  and the spin rate  $\mathbf{w}$

$$\mathbf{d} = \frac{1}{2}[\mathbf{l} + \mathbf{l}^T] \quad \text{and} \quad \mathbf{w} = \frac{1}{2}[\mathbf{l} - \mathbf{l}^T] \quad (10)$$

This decomposition is useful for brain tissue for which the viscous spin rate is often assumed to vanish [14–16],  $\mathbf{w} = \mathbf{0}$ , as we will see in Sec. 5.4.

Large deformations of biological tissues are often characterized in terms of stretches instead of strains [17]. The stretches  $\lambda_1, \lambda_2$ , and  $\lambda_3$  follow uniquely from the spectral decomposition of the left and right Cauchy-Green deformation tensors:

$$\mathbf{b} = \sum_{i=1}^3 \lambda_i^2 \mathbf{n}_i \otimes \mathbf{n}_i \quad \text{and} \quad \mathbf{C} = \sum_{i=1}^3 \lambda_i^2 \mathbf{N}_i \otimes \mathbf{N}_i \quad (11)$$

where  $\mathbf{n}_i$  and  $\mathbf{N}_i$  are the eigenvectors of  $\mathbf{b}$  and  $\mathbf{C}$ , and  $\lambda_i^2$  are the corresponding eigenvalues, which are real and positive by definition of  $\mathbf{b}$  and  $\mathbf{C}$ . Similarly, we can rewrite the deformation gradient  $\mathbf{F}$  in terms of the eigenvectors  $\mathbf{n}_i$  and  $\mathbf{N}_i$  and the stretches  $\lambda_i$

$$\mathbf{F} = \sum_{i=1}^3 \lambda_i \mathbf{n}_i \otimes \mathbf{N}_i \quad (12)$$

In many constitutive models for hyperelastic materials, the invariants of the deformation tensors  $\mathbf{b}$  and  $\mathbf{C}$  (5) are expressed in terms of the stretches  $\lambda_i$

$$\begin{aligned} I_1 &= \lambda_1^2 + \lambda_2^2 + \lambda_3^2 \\ I_2 &= \lambda_1^2 \lambda_2^2 + \lambda_2^2 \lambda_3^2 + \lambda_1^2 \lambda_3^2 \\ J^2 &= I_3 = \lambda_1^2 \lambda_2^2 \lambda_3^2 \end{aligned} \quad (13)$$

To obtain the derivative of the stretches with respect to the Cauchy-Green deformation tensors  $\mathbf{b}$  and  $\mathbf{C}$ , we use the spectral decomposition (11) and recall that  $\mathbf{b}$  and  $\mathbf{C}$  are real and symmetric, such that

$$\frac{\partial \lambda_i^2}{\partial \mathbf{b}} = \mathbf{n}_i \otimes \mathbf{n}_i \quad \text{and} \quad \frac{\partial \lambda_i^2}{\partial \mathbf{C}} = \mathbf{N}_i \otimes \mathbf{N}_i \quad i = 1, 2, 3 \quad (14)$$

A relation that will be useful for the brain models in Sec. 3 follows from using Eq. (14) together with the chain rule:

$$\frac{\partial \lambda_i^2}{\partial \mathbf{C}} = \frac{\alpha}{2} \lambda_i^{\alpha-2} \mathbf{N}_i \otimes \mathbf{N}_i \quad i = 1, 2, 3 \quad (15)$$

The deformation of anisotropic materials is usually characterized by the fourth and fifth invariants,  $I_4$  and  $I_5$  [18]

$$\begin{aligned} I_4 &= \mathbf{M} \cdot \mathbf{C} \cdot \mathbf{M} = \lambda_M^2 \\ I_5 &= \mathbf{M} \cdot \mathbf{C}^2 \cdot \mathbf{M} \end{aligned} \quad (16)$$

where  $\mathbf{M}$  is the preferred direction in the reference configuration, e.g., the axon orientation, and  $\lambda_M$  is the stretch in this direction, e.g., the axonal stretch. In brain tissue,  $I_4$  represents anisotropy due to deformation of the axons, and  $I_5$  describes the anisotropy of matrix–fiber interactions [19]. Both anisotropic deformation modes,  $I_4$  and  $I_5$ , have been demonstrated to have an effect on experimental results for brain tissue indentation [20].

In general, stretch-based formulations can be superior to invariant-based formulations, since they might allow for a more straightforward interpretation of the constitutive behavior, especially in homogeneous experimental settings such as uniaxial tension or simple shear.

**2.1.1 Incompressibility.** A widely used and very common assumption is to postulate that soft biological tissues, including the brain, are incompressible. Incompressibility manifests itself through a constant Jacobian,  $J = \det(\mathbf{F}) = 1$ , which implies that the invariants for an incompressible material simplify to

$$\begin{aligned} I_1 &= \bar{I}_1 = \lambda_1^2 + \lambda_2^2 + \lambda_3^2 \\ I_2 &= \bar{I}_2 = \lambda_1^{-2} + \lambda_2^{-2} + \lambda_3^{-2} \\ J^2 &= I_3 = \bar{I}_3 = 1 \end{aligned} \quad (17)$$

Only a few approaches have modeled brain tissue as a compressible material. In the case of compressibility, Poisson's ratio was measured as  $\nu_{\text{dry}} = 0.4$  for dry brain tissue [21] and  $\nu_{\text{wet}} = 0.496$  for wet brain tissue [22]. The wet tissue value is very close to the incompressibility limit of  $\nu = 0.5$ , which suggests that the incompressible cerebrospinal fluid dominates the behavior of brain tissue. In the literature, the assumption of incompressibility commonly refers to wet brain tissue. Only in multiphase formulations, when the fluid is considered separately from the dry tissue, the tissue is assumed to be compressible. The notion of compressibility becomes slightly ambiguous when considering the time-dependent properties of brain tissue. In this review, we refer to incompressibility as being equivalent to an infinite bulk modulus. The porous nature of brain tissue may cause an apparent compressibility when fluid locally migrates into or out of the tissue.

**2.2 Special Cases.** Two special cases of deformation are worth mentioning as they are often used experimentally to directly calibrate and validate constitutive brain models. These special cases are incompressible, uniaxial tension/compression and simple shear [23].

**2.2.1 Incompressible, Uniaxial Tension/Compression.** The deformation gradient for incompressible, uniaxial tension/compression along one-direction is

$$\mathbf{F} = \begin{bmatrix} \lambda & 0 & 0 \\ 0 & \lambda^{-1/2} & 0 \\ 0 & 0 & \lambda^{-1/2} \end{bmatrix} \quad (18)$$

Incompressibility follows from Eq. (18) as  $J = \det(\mathbf{F}) = 1$ . The left and right Cauchy-Green deformation tensors become

$$\mathbf{b} = \mathbf{C} = \begin{bmatrix} \lambda^2 & 0 & 0 \\ 0 & \lambda^{-1} & 0 \\ 0 & 0 & \lambda^{-1} \end{bmatrix} \quad (19)$$

The three stretches for uniaxial tension/compression are  $\lambda_1 = \lambda$  and  $\lambda_2 = \lambda_3 = \lambda^{-1/2}$ , and the corresponding eigenvectors are  $\mathbf{n}_i = \mathbf{N}_i = \mathbf{e}_i$  for  $i = 1, 2, 3$ , where  $\mathbf{e}_i$  is the set of Cartesian basis vectors. The stretches define the invariants (17) of incompressible, uniaxial tension/compression

$$I_1 = \lambda^2 + 2\lambda^{-1}, \quad I_2 = 2\lambda + \lambda^{-2}, \quad \text{and} \quad I_3 = 1 \quad (20)$$

The stretches and deformation tensors define the expression

$$\mathbf{I}_1 \mathbf{b} - \mathbf{b}^2 = \begin{bmatrix} 2\lambda & 0 & 0 \\ 0 & \lambda + \lambda^{-2} & 0 \\ 0 & 0 & \lambda + \lambda^{-2} \end{bmatrix} \quad (21)$$

which will become important to derive stresses of incompressible brain tissue under uniaxial loading in Sec. 3.

**2.2.2 Simple Shear.** The deformation gradient for simple shear along the one-two-direction is

$$\mathbf{F} = \begin{bmatrix} 1 & \gamma & 0 \\ 0 & 1 & 0 \\ 0 & 0 & 1 \end{bmatrix} \quad (22)$$

in which  $\gamma$  is the shear angle. By definition, simple shear is an incompressible deformation as  $J = \det(\mathbf{F}) = 1$ . The left and right deformation tensors become

$$\mathbf{b} = \begin{bmatrix} 1 + \gamma^2 & \gamma & 0 \\ \gamma & 1 & 0 \\ 0 & 0 & 1 \end{bmatrix} \quad \text{and} \quad \mathbf{C} = \begin{bmatrix} 1 & \gamma & 0 \\ \gamma & 1 + \gamma^2 & 0 \\ 0 & 0 & 1 \end{bmatrix} \quad (23)$$

The stretches are  $\lambda_1 = \lambda$ ,  $\lambda_2 = 1/\lambda$ , and  $\lambda_3 = 1$ , with  $\gamma = \lambda - 1/\lambda$  and the invariants become

$$I_1 = I_2 = \lambda^2 + \lambda^{-2} + 1 = 3 + \gamma^2 \quad \text{and} \quad I_3 = 1 \quad (24)$$

Finally, we provide the expression

$$\mathbf{I}_1 \mathbf{b} - \mathbf{b}^2 = \begin{bmatrix} 2 + \gamma^2 & \gamma & 0 \\ \gamma & 2 & 0 \\ 0 & 0 & 2 + \gamma^2 \end{bmatrix} \quad (25)$$

to derive tissue stresses under simple shear loading.

### 3 Finite Hyperelasticity

An important contribution to constitutive models for brain tissue is the characterization of the elastic, time-independent material response. This elastic response of brain tissue is often modeled as hyperelastic. Indeed, for many common loading conditions, the elastic behavior of the brain resembles that of hyperelastic, rubberlike materials [22,23]. In this section, we present a general overview of constitutive models for this class of materials. In Sec. 3.1, we reiterate several theoretical considerations for incompressible, hyperelastic materials. In Sec. 3.2, we introduce popular baseline constitutive models that are often used for soft materials. In Sec. 3.3, we consider the treatment of compressibility for hyperelastic materials.

**3.1 Incompressibility.** Most constitutive models define the elastic material response of brain tissue as hyperelastic. By definition, this implies that we can characterize the material by a hyperelastic strain energy function  $\Psi$  that maps the deformation to a strain energy potential. Material objectivity requires that  $\Psi$  depends on the deformation through the right Cauchy-Green deformation tensor  $\mathbf{C}$  only. This implies that we can express the strain energy function in terms of the invariants  $I_1$ ,  $I_2$ , and  $I_3$  (13). Unless stated otherwise in Sec. 3.3, we assume that brain tissue is incompressible,  $I_3 = 1$ , and that its strain energy function  $\Psi$  depends only on the first two invariants

$$\Psi(\mathbf{C}) = \Psi(I_1, I_2) \quad (26)$$

The hyperelastic strain energy (26) defines the Cauchy stress  $\boldsymbol{\sigma}$ , the current force per unit area, which describes the true stress state in the material. For incompressible materials, the Cauchy stress follows from the strain energy function as:

$$\boldsymbol{\sigma} = -p\mathbf{I} + 2J^{-1}\mathbf{F} \cdot \frac{\partial \Psi}{\partial \mathbf{C}} \cdot \mathbf{F}^T \quad (27)$$

in which  $p$  is the hydrostatic pressure that is determined by the boundary conditions. Using the chain rule and Eq. (5), we can rewrite the stress tensor as

$$\boldsymbol{\sigma} = -p\mathbf{I} + 2\frac{\partial\Psi}{\partial I_1}\mathbf{b} + 2\frac{\partial\Psi}{\partial I_2}(I_1\mathbf{b} - \mathbf{b}^2) \quad (28)$$

In some cases, it proves convenient to use the Cayley–Hamilton theorem for incompressible deformations,  $I_1\mathbf{b} - \mathbf{b}^2 = I_2\mathbf{I} - \mathbf{b}^{-1}$ , and rewrite the Cauchy stress as

$$\boldsymbol{\sigma} = -p^*\mathbf{I} + 2\frac{\partial\Psi}{\partial I_1}\mathbf{b} - 2\frac{\partial\Psi}{\partial I_2}\mathbf{b}^{-1} \quad (29)$$

where  $p^* = p - 2I_2\partial\Psi/\partial I_2$ . Here, the term  $-p\mathbf{I}$  does not necessarily represent the total hydrostatic pressure, since the other contributions in Eq. (28) may also contain some volumetric contributions.

**3.2 Baseline Constitutive Models.** In this section, we summarize some widely used strain energy functions for hyperelastic materials. We also illustrate the stress–stretch relation between  $\sigma_{11}$  and  $\lambda$  for the special case of uniaxial tension/compression highlighted in Sec. 2.2.1. This stress–stretch relation is important, since it is commonly used to calibrate constitutive models via uniaxial tension/compression experiments.

**3.2.1 Ogden Model.** One of the most popular strain energy functions for soft biological tissues is adopted from rubberlike materials based on the hyperelastic Ogden model [17,24]

$$\Psi^{\text{ogd}} = \sum_{i=1}^N \frac{\mu_i}{\alpha_i} [\lambda_1^{\alpha_i} + \lambda_2^{\alpha_i} + \lambda_3^{\alpha_i} - 3] \quad (30)$$

in which  $N$ ,  $\mu_i$ , and  $\alpha_i$  are the material parameters. The shear modulus at infinitesimal strains  $\mu$  is related to these parameters as  $2\mu = \sum_{i=1}^N \mu_i \alpha_i$ . We obtain the Cauchy stress tensor for the Ogden model by combining Eqs. (15), (27), and (30)

$$\boldsymbol{\sigma}^{\text{ogd}} = -p\mathbf{I} + \sum_{i=1}^N \mu_i [\lambda_1^{\alpha_i} \mathbf{n}_1 \otimes \mathbf{n}_1 + \lambda_2^{\alpha_i} \mathbf{n}_2 \otimes \mathbf{n}_2 + \lambda_3^{\alpha_i} \mathbf{n}_3 \otimes \mathbf{n}_3] \quad (31)$$

For the special case of incompressible, uniaxial tension/compression according to Eq. (18),  $\boldsymbol{\sigma}^{\text{ogd}} = -p\mathbf{I} + \sum_{i=1}^N \mu_i [\lambda^{\alpha_i} \mathbf{e}_1 \otimes \mathbf{e}_1 + \lambda^{-\alpha_i/2} (\mathbf{e}_2 \otimes \mathbf{e}_2 + \mathbf{e}_3 \otimes \mathbf{e}_3)]$ , and the pressure  $p$  follows by solving  $\sigma_{22} = \sigma_{33} = 0$ . Substituting these special-case conditions into the general stress definition (31) yields the uniaxial stress–stretch relation of the Ogden model

$$\sigma_{11}^{\text{ogd}} = \sum_{i=1}^N \mu_i [\lambda^{\alpha_i} - \lambda^{-\alpha_i/2}] \quad (32)$$

**3.2.2 Mooney–Rivlin Model.** A special case of the Ogden model is the incompressible Mooney–Rivlin model [25,26], which follows by choosing  $N = 2$ ,  $\alpha_1 = 2$ , and  $\alpha_2 = -2$ , such that:

$$\begin{aligned} \Psi^{\text{mr}} &= \frac{1}{2} \mu_1 [\lambda_1^2 + \lambda_2^2 + \lambda_3^2 - 3] - \frac{1}{2} \mu_2 [\lambda_1^{-2} + \lambda_2^{-2} + \lambda_3^{-2} - 3] \\ &= \frac{1}{2} \mu_1 [I_1 - 3] - \frac{1}{2} \mu_2 [I_2 - 3] \end{aligned} \quad (33)$$

To convert the stretch-based formulation (the first of Eq. (33)) into the invariant-based formulation (the second of Eq. (33)), we have applied the incompressibility assumption. The coefficients  $\mu_1$  and  $\mu_2$  are related to the shear modulus as  $\mu = \mu_1 - \mu_2$ . We obtain the uniaxial stress–stretch relation for the Mooney–Rivlin model by substituting the values for  $N$ ,  $\alpha_1$ , and  $\alpha_2$  into the uniaxial Ogden model in Eq. (32)

$$\sigma_{11}^{\text{mr}} = \mu_1 [\lambda^2 - \lambda^{-1}] + \mu_2 [\lambda^{-2} - \lambda] \quad (34)$$

**3.2.3 Neo-Hookean Model.** The widely used Neo-Hookean material model also follows as a special case of the Ogden and Mooney–Rivlin models by choosing  $N = 1$  and  $\alpha_1 = 2$ :

$$\Psi^{\text{nh}} = \frac{1}{2} \mu [\lambda_1^2 + \lambda_2^2 + \lambda_3^2 - 3] = \frac{1}{2} \mu [I_1 - 3] \quad (35)$$

The Neo-Hookean model consists of a single material parameter  $\mu$ , which is associated with the shear modulus in the linear regime. The Neo-Hookean stress

$$\boldsymbol{\sigma}^{\text{nh}} = -p\mathbf{I} + \mu\mathbf{b} \quad (36)$$

reduces to the uniaxial stress–stretch relation for the Neo-Hookean model by using Eq. (19) and substituting the pressure  $p$ , or simply by dropping the second term in the Mooney–Rivlin model (34)

$$\sigma_{11}^{\text{nh}} = \mu [\lambda^2 - \lambda^{-1}] \quad (37)$$

**3.2.4 Linear Elastic Model.** The linear elastic model is a special case of the hyperelastic model (35), in which the stress–strain relation is linear. This model is only valid in the linear regime, which several studies report as low as 0.1% of strain for brain tissue [6]. The strain energy function for linear elastic materials takes the form

$$\Psi^{\text{lin}} = \frac{1}{2} L \text{tr}^2(\boldsymbol{\varepsilon}) + \frac{1}{2} \mu \text{tr}(\boldsymbol{\varepsilon}^2) \quad (38)$$

in which  $L$  and  $\mu$  are the Lamé constants,  $\boldsymbol{\varepsilon} = \nabla^{\text{sym}}\mathbf{u}$  is the linearized strain tensor, and  $\mathbf{u} = \boldsymbol{\phi} - \mathbf{X}$  is the displacement vector. In general, Eq. (38) represents a compressible material, and incompressibility would be represented by  $L \rightarrow \infty$ . The stress tensor for the compressible linear elastic model follows as:

$$\boldsymbol{\sigma}^{\text{lin}} = \frac{\partial\Psi^{\text{lin}}}{\partial\boldsymbol{\varepsilon}} = L \text{tr}(\boldsymbol{\varepsilon})\mathbf{I} + 2\mu\boldsymbol{\varepsilon} \quad (39)$$

where the first term differs from Eq. (36) because of the compressible nature of Eq. (39), and the second term,  $2\mu\boldsymbol{\varepsilon}$ , is the linearized version of  $\mu\mathbf{b}$ . The stress–strain relation for uniaxial loading is widely known as Hooke’s law

$$\sigma_{11}^{\text{lin}} = E\varepsilon_{11} = E[\lambda - 1] \quad (40)$$

in which  $E = \mu[3L + 2\mu]/[L + \mu]$  is the Young’s modulus.

**3.2.5 Polynomial Model.** A variation on the Mooney–Rivlin model is the polynomial model [27], which contains the Mooney–Rivlin model as a the special case with  $N = 1$

$$\Psi^{\text{pol}} = \sum_{i+j=1}^N \mu_{ij} [I_1 - 3]^i [I_2 - 3]^j \quad (41)$$

The Cauchy stress for the polynomial model is derived from Eq. (41) using Eq. (28)

$$\begin{aligned} \boldsymbol{\sigma}^{\text{pol}} &= -p\mathbf{I} + \sum_{i+j=1}^N 2\mu_{ij} [i [I_1 - 3]^{i-1} [I_2 - 3]^j \mathbf{b} \\ &\quad + j [I_1 - 3]^i [I_2 - 3]^{j-1} [I_1\mathbf{b} - \mathbf{b}^2]] \end{aligned} \quad (42)$$

with  $I_1$  and  $I_2$  as in Eq. (20). Solving for the pressure  $p$  with  $\sigma_{22} = \sigma_{33} = 0$  and substituting the result into Eq. (42) yield the stress–stretch relation for the polynomial model

$$\begin{aligned} \sigma_{11}^{\text{pol}} &= \sum_{i+j=1}^N 2\mu_{ij} [i [I_1 - 3]^{i-1} [I_2 - 3]^j [\lambda^2 - \lambda^{-1}] \\ &\quad + j [I_1 - 3]^i [I_2 - 3]^{j-1} [\lambda - \lambda^{-2}]] \end{aligned} \quad (43)$$

**3.2.6 Gent Model.** Some rubberlike materials exhibit a deformation limit at which the stresses increase to infinity. This phenomenon is captured by the Gent model [28]

$$\begin{aligned}\Psi^{\text{ent}} &= -\frac{\mu}{2\beta} \ln\left(1 - \beta[\lambda_1^2 + \lambda_2^2 + \lambda_3^2 - 3]\right) \\ &= -\frac{\mu}{2\beta} \ln(1 - \beta[I_1 - 3])\end{aligned}\quad (44)$$

The material parameter  $\beta$  is a measure of the deformation limit as  $\beta = 1/[I_1^{\text{lim}} - 3]$ . We derive the Cauchy stress for the Gent model from Eqs. (28) and (44)

$$\boldsymbol{\sigma}^{\text{ent}} = -p\mathbf{I} + \frac{\mu}{1 - \beta[I_1 - 3]} \mathbf{b} \quad (45)$$

With  $\sigma_{22} = \sigma_{33} = 0$ , we obtain the uniaxial stress–stretch relation for the Gent model

$$\sigma_{11}^{\text{ent}} = \frac{\mu}{1 - \beta[I_1 - 3]} (\lambda^2 - \lambda^{-1}) \quad (46)$$

If the deformation limit approaches infinity,  $I_1^{\text{lim}} \rightarrow \infty$ , the limit parameter vanishes,  $\beta \rightarrow 0$ , and the Gent model simplifies to the Neo-Hookean model in Eqs. (36) and (37).

**3.2.7 Holzapfel Model.** All the previous models assume that the brain tissue is isotropic and possesses no pronounced material direction. Soft biological tissues, however, are often anisotropic, for example, caused by one-dimensional fibers, such as axon fiber bundles in the white matter brain tissue [29]. The Holzapfel model [30] allows to account for tissue anisotropy by supplementing the free energy function with an additional term, which accounts for the anisotropic material response

$$\Psi^{\text{hlz}} = \Psi^{\text{iso}} + \frac{k_1}{k_2} \left[ \exp\left(k_2 [I_4 - 1]^2\right) - 1 \right] \quad (47)$$

in which  $\Psi^{\text{iso}}$  is any isotropic strain energy function,  $k_1$  and  $k_2$  are the material parameters with the dimension of stress and without dimension, respectively, and  $I_4$  is the fourth invariant as in Eq. (16). In essence, the Holzapfel model adds a Fung-type exponential stiffness term along the direction  $\mathbf{M}$ . We obtain the Cauchy stress for the Holzapfel model using Eq. (27)

$$\begin{aligned}\boldsymbol{\sigma}^{\text{hlz}} &= -p\mathbf{I} + 2\mathbf{F} \cdot \frac{\partial \Psi^{\text{iso}}}{\partial \mathbf{C}} \cdot \mathbf{F}^T \\ &\quad + 2k_1 [I_4 - 1] \exp\left(k_2 [I_4 - 1]^2\right) \mathbf{m} \otimes \mathbf{m}\end{aligned}\quad (48)$$

where  $\mathbf{m} = \mathbf{F} \cdot \mathbf{M}$  is the preferred direction in the deformed configuration. In the case of uniaxial tension with anisotropy along the loading direction, the preferred direction,  $\mathbf{M} = \mathbf{e}_1$ , is simply stretched into the current configuration,  $\mathbf{m} = \lambda \mathbf{e}_1$ , and the uniaxial stress–stretch relation of the Holzapfel model becomes

$$\sigma_{11}^{\text{hlz}} = \sigma_{11}^{\text{iso}} + 2k_1 [I_4 - 1] \exp(k_2 [I_4 - 1]^2) \lambda^2 \quad (49)$$

The isotropic term  $\sigma_{11}^{\text{iso}}$  is the stress during incompressible, uniaxial tension/compression obtained from  $\Psi^{\text{iso}}$ , which could, e.g., be any of the models discussed earlier in this section. To expand the anisotropic term of the model beyond a single preferred direction, we could generalize the standard Holzapfel model to account for a spatially distributed preferred direction based on a probability distribution function [31].

In this section, we have presented six different widely used constitutive models for hyperelastic materials together with their stress–stretch relations for uniaxial tension and compression. Figure 1 illustrates the characteristic features and differences of these constitutive models for uniaxial loading and simple shear. We chose the material parameters such that the initial shear modulus  $\mu$  is the same for all models and that the material response is consistent with experimental data for brain tissue. Figure 1 suggests that all the models capture a similar behavior in the

infinitesimal deformation regime, top, but display significant differences in the finite deformation setting, bottom.

**3.3 Compressibility.** Although most constitutive models assume that brain tissue is incompressible, some models do not feature this assumption [16,32,33]. In this section, we briefly discuss an approach for modeling brain tissue as a compressible material. In general, the Jacobian of compressible materials is nonconstant,  $J \neq 1$ , and the strain energy function explicitly depends on  $J$

$$\Psi(C) = \Psi(J, \bar{I}_1, \bar{I}_2) \quad (50)$$

where  $\bar{I}_1$  and  $\bar{I}_2$  are the isochoric invariants (7). A common approach is to additively decompose the strain energy function into its volumetric or shape preserving part  $U(J)$  and its deviatoric or volume preserving part  $\bar{\Psi}(\bar{I}_1, \bar{I}_2)$

$$\Psi(J, \bar{I}_1, \bar{I}_2) = U(J) + \bar{\Psi}(\bar{I}_1, \bar{I}_2) \quad (51)$$

The deviatoric energy,  $\bar{\Psi}(\bar{I}_1, \bar{I}_2)$ , can be any of the strain energy functions in Sec. 3.2 with  $I_1$  and  $I_2$  replaced by  $\bar{I}_1$  and  $\bar{I}_2$ . The volumetric energy,  $U(J)$  could, for example, be chosen according to the volumetric Ogden model [17]

$$U^{\text{ogd}}(J) = \frac{1}{\beta^2} K [J^{-\beta} - 1 + \beta \ln(J)] \quad (52)$$

where  $K$  is the bulk modulus, and  $\beta$  is an additional material parameter. The volumetric Ogden model (52) is a generalization of the volumetric Simo-Miehe model [34] for  $\beta = 2$

$$U^{\text{smo}}(J) = \frac{1}{2} K \left[ \frac{1}{2} [J^2 - 1] - \ln(J) \right] \quad (53)$$

The volumetric Neo-Hookean model, the simplest volumetric model, is exclusively based on a single quadratic term

$$U^{\text{nh}}(J) = \frac{1}{2} K [J - 1]^2 \quad (54)$$

The Ogden term (52), the Simo-Miehe term (53), and the Neo-Hookean term (54) are equivalent up to third order,  $O([J - 1]^3)$ .

## 4 Time-Independent Modeling of Brain Tissue

The viscoelastic nature of brain tissue has been recognized from the early days of material testing [7,35,36]. Constitutive relations for viscoelastic materials consist of a time-independent elastic contribution and a time-dependent viscous contribution. In this section, we review the constitutive modeling of the time-independent response of brain tissue. We will frequently refer to the previous section, since many constitutive models for brain tissue are motivated by the general hyperelastic material models for rubberlike materials in Sec. 3.

**4.1 Magnetic Resonance Elastography Models.** Recent advances in magnetic resonance elastography to measure tissue properties in vivo [37–39] have led to an increased popularity of the linear elastic model described in Sec. 3.2. Indeed, magnetic resonance elastography is inherently based on the assumption of linear elasticity [40]. Although limited to the small strain regime [6], magnetic resonance elastography provides valuable insight into many long-term, low-strain phenomena, such as aging [41] or multiple sclerosis [42]. Because of its noninvasive nature, magnetic resonance elastography is an extremely valuable diagnostic tool to measure *changes* in brain properties as indicators for neurological disorders or diseases. Additionally, material properties obtained from magnetic resonance elastography of the living brain provide valuable guidelines for the in vivo material parameters for

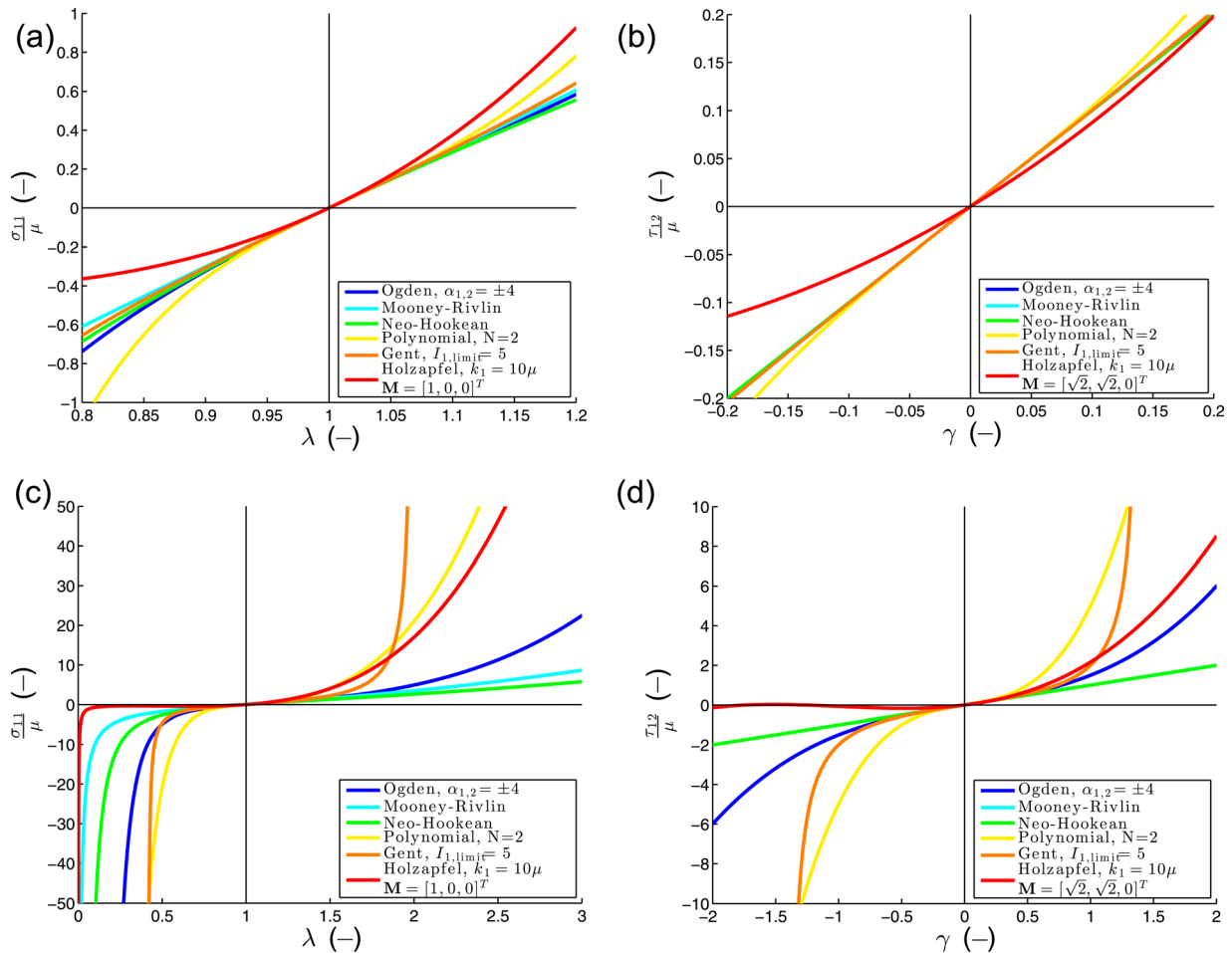


**Fig. 1** Special cases of incompressible, uniaxial tension/compression (left) and simple shear (right) for different hyperelastic brain tissue models. The top and bottom figures illustrate the responses for small and large deformations. The material parameters are chosen such that  $\partial\sigma_{11}/\partial\lambda|_{\lambda=1}$  is the same for all the models. The remaining material parameters are chosen to be consistent with the experimental data.

constitutive models; they can even be used to calibrate nonlinear finite deformation models in the low-strain limit.

**4.2 Mendis and Miller Models.** The polynomial model of Sec. 3.2 is often used to describe the incompressible, hyperelastic behavior of brain tissue. Several groups have successfully adopted the polynomial model in Eq. (41) with  $N=2$ , which results in five material parameters to model the time-independent elastic response [33,43–46].

**4.3 Miller and Prange Models.** The polynomial model was later abandoned since it fails to capture the different behaviors in tension and compression [47]. It was replaced by the Ogden model (30). The two parameters  $\mu_1$  and  $\alpha_1$  of the one-term,  $N=1$ , Ogden model were calibrated individually using the experimental data for tension, shear, and confined compression [47–50]. Using a two-term,  $N=2$ , Ogden model, recent more advanced studies performed model calibrations for the four Ogden parameters  $\mu_1$ ,  $\mu_2$ ,  $\alpha_1$ , and  $\alpha_2$  under cyclic tension/compression loading [22].

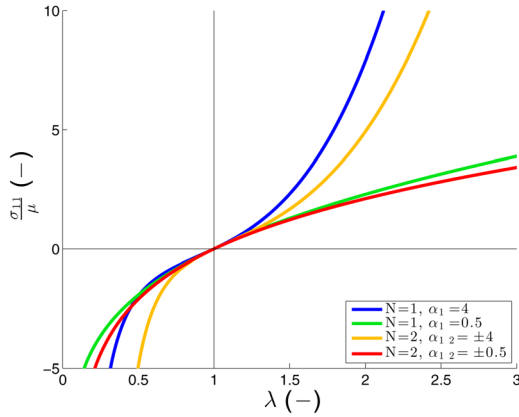
Figure 2 illustrates the sensitivity of the Ogden model for varying  $\alpha$  values. The Ogden model is a phenomenological model, which has been criticized for using material parameters that have no real physical interpretation. Yet, its behavior is highly sensitive to these phenomenological parameters: In the tensile regime, the model displays strain softening if the magnitude of all  $\alpha$  parameters is smaller than one,  $|\alpha_i| < 1$  for all  $i = 1 \dots N$ , and strain hardening otherwise.

Table 1 summarizes the different  $\alpha_i$  values reported in the literature. These values show large discrepancies, even within the same reference. The  $\alpha$  values in the third row even suggests a strain-softening behavior [48], whereas the  $\alpha$  values in all other reports suggest strain-hardening [22,47,49]. These different findings could be caused by different types of preconditioning [22]. Other potential sources for this discrepancy are differences in experimental setups, approximation methods, or simply a low sensitivity to the value of  $\alpha_i$  [9]. The latter would explain that the Mooney–Rivlin and Neo-Hookean models—although much simpler—are still widely used for modeling the elastic behavior of brain tissue.

**4.4 Cloots Model.** The Neo-Hookean model was one of the first constitutive models for brain tissue [51] and it is still frequently used today [52]. The Cloots model [32] for diffuse axonal injury combines the incompressible Neo-Hookean model (35), the compressible Simo-Miehe model (53), and Holzapfel model (47) from Sec. 3.2

$$\Psi^{\text{cl}} = \mu [\bar{I}_1 - 3] + \frac{1}{2} K \left[ \frac{1}{2} [J^2 - 1] - \ln(J) \right] + \frac{k_1}{k_2} \left[ \exp \left( k_2 [I_4 - 1]^2 \right) - 1 \right] \quad (55)$$

For the suggested bulk modulus of  $K=2.5$  GPa combined with a tissue modulus of up to  $\mu=150$  Pa in the preferred direction,



**Fig. 2** Axial stress versus stretch curves for the Ogden model in incompressible, uniaxial tension/compression loading for varying model parameters  $N$  and  $\alpha_i$ . In tension, the Ogden model displays a strain softening if  $|\alpha_i| < 1$  for all  $i = 1 \dots N$ , and a strain stiffening otherwise. In compression, the model predicts a strain stiffening for all the values of  $\alpha_i$ .

**Table 1** Experimental values for  $\alpha_i$  in Ogden model

	$\alpha_1$	$\alpha_2$
Franceschini et al. [22]	-10.8, 23.5	19.7, -4.0
Miller and Chinzei [47]	-4.7	N/A
Prange and Margulies [48]	0.01-0.06	N/A
Rashid et al. [49]	2.5-4.8	N/A

the material behavior is nearly incompressible with  $\nu = (3K - 2\mu)/(6K + 2\mu) = 0.5$ .

**4.5 Hrapko Model.** The Hrapko model [15] represents the brain tissue as a rheological system of parallel springs and dampers. It uses two different strain energy functions to characterize the constitutive behavior of the springs,  $\Psi^{\text{hr1}}$  and  $\Psi^{\text{hr2}}$ . The first Hrapko function uses a combination of the Mooney–Rivlin and Neo-Hookean models [15]

$$\Psi^{\text{hr1}} = \frac{1}{2} \mu [aI_1 + [1 - a]I_2 - 3] \quad (56)$$

For  $a = 1$ , in the case of pure shear with  $I_1 = I_2$ , the Hrapko model reduces to the Neo-Hookean model, see Sec. 2.2.2. The second Hrapko function is slightly more complex and features two additional parameters to better fit the constitutive behavior [15]

$$\Psi^{\text{hr2}} = \frac{1}{2} \mu A x^2 - \frac{1}{C^2} \mu [1 - A] [[Cx + 1] \exp(-Cx) - 1] \quad (57)$$

The term  $x(I_1, I_2) = \sqrt{aI_1 + [1 - a]I_2 - 3}$  weights the influence of the first and second invariants,  $I_1$  and  $I_2$ . The weighting factor  $a$  plays a similar role as in the first Hrapko function (56).

**4.6 Bilston Model.** The Bilston model [14] uses a similar approach as the Hrapko model [15]

$$\Psi^{\text{bil}} = \mu \frac{I_1 + aI_2 - 3}{1 + a} [[C_1 x]^{p_1} + 1]^{m-1/2} \exp([-C_2 x]^{p_2}) \quad (58)$$

The weighting term  $x(I_1, I_2) = \sqrt{aI_1 + [1 - a]I_2 - 3}$  is similar to the Hrapko model (57). The parameters  $C_1$  and  $C_2$  are similar to the single parameter  $C$  in the Hrapko model, and  $p_1$ ,  $p_2$ , and  $m$  are the additional material parameters. Although the Bilston model [14] and the Hrapko model [15] are not entirely identical, their approaches are both motivated by polymeric materials:

The choice of  $x(I_1, I_2)$  in Eq. (57) is based on a constitutive model for polyethylene melts [53], which models the individual response of polymers under shear and tensile loading. The nonlinear function  $[[C_1 x]^{p_1} + 1]^{m-1/2} \exp([-C_2 x]^{p_2})$  in Eq. (58) is based on a constitutive model for dough [54], which consists of a network of long-chain polymers with permanent crosslinks. The values of  $C_1$  and  $C_2$  are the thresholds for the polynomial and exponential behavior of this function.

**4.7 Prevost Model.** All the constitutive models considered so far are phenomenological in nature. The Prevost model [16] is a micromechanically motivated viscoelastic model with a deviatoric elastic contribution motivated by the eight-chain Arruda–Boyce model [55] for macromolecular elastic networks

$$\bar{\Psi}^{\text{prv}} = 2\mu \frac{1}{J} \left[ \frac{\lambda}{\lambda_L} \mathcal{L}^{-1}(\lambda/\lambda_L) + \ln \frac{\mathcal{L}^{-1}(\lambda/\lambda_L)}{\sinh \mathcal{L}^{-1}(\lambda/\lambda_L)} \right] \quad (59)$$

where  $\bar{\Psi}$  is the volumetric strain energy (51),  $\bar{\mathbf{b}}$  is the isochoric left Cauchy–Green deformation tensor (6),  $J = \det(\mathbf{F})$  is the Jacobian,  $\lambda = \sqrt{I_1}/3$  is a measure of the stretch,  $\lambda_L$  is the locking stretch, and  $\mathcal{L}(\lambda/\lambda_L)$  is the Langevin function with  $\mathcal{L}(\lambda/\lambda_L) = \coth(\lambda/\lambda_L) - \lambda_L/\lambda$ . Equation (59) models the brain tissue using a statistical mechanics approach of a network of eight polymer chains in a cube. In addition, the Prevost model assumes the following equation for the hydrostatic pressure [16]:

$$p^{\text{prv}} = -K \ln \left( \frac{J - f_1}{1 - f_1} \right) \quad (60)$$

in which  $K$  is the bulk modulus, and  $f_1$  denotes the fraction of incompressible volume. For the brain tissue, this incompressible volume fraction is on the order of  $f_1 = 0.8$ . The fit for this model with experimental data yields bulk moduli on the order of  $K = 2 \times 10^2 - 2 \times 10^4$  Pa and shear moduli on the order of  $\mu = 5 - 100$  Pa. These parameter ranges translate into a Poisson’s ratio of  $\nu = 0.48 - 0.50$ , which again confirms the near-incompressibility of the brain tissue.

**4.8 Ahmadzadeh Model.** The previous models in this section were motivated by micromechanical considerations of long-chain molecules [14–16]. An alternative approach is to explicitly model the discrete microstructure of the brain tissue [56]. This type of mechanistic, physics-based constitutive models represents axons discretely as networks of microtubules, modeled as elastic rods, which are cross-linked by tau-proteins, modeled as springs [57]. This discrete approach results in a one-dimensional constitutive model for individual axons, which could eventually be embedded into a three-dimensional continuum model at the tissue level [29].

## 5 Time-Dependent Modeling of Brain Tissue

In this section, we review the modeling of the time-dependent material response of the brain tissue. In tissue rheology, time-dependent properties are often simply referred to as viscoelastic properties. However, it should be noted that the time dependency of the response is not just due to viscous effects alone, but also a result of other time-depending phenomena including porous effects. Here, we therefore refer to the response as time-dependent, rather than viscous. Figure 3 illustrates our experimentally measured time-dependent behavior of the brain tissue under uniaxial loading. Gray and white matter tissue display viscous effects and stress relaxation under constant deformation.

**5.1 Multiphase Models.** Brain tissue is highly complex in nature, and its mechanical response may be affected by multiple physical phases, including the solid, fluid, and charged ions. For example, viscous effects are due to the solid phase, whereas porous effects are attributed to movement of the cerebral spinal fluid.

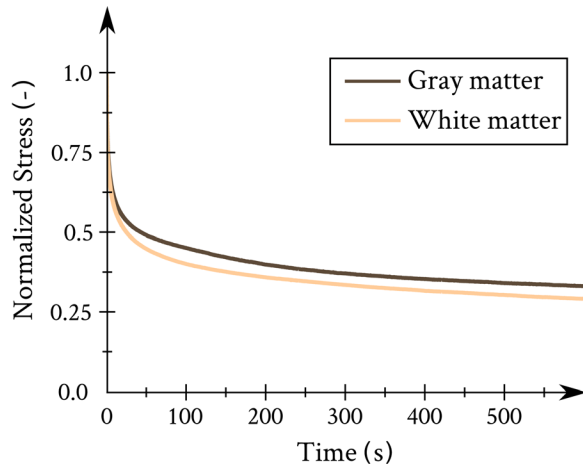


**Fig. 3 Time-dependent behavior of the brain tissue under uniaxial loading. The brain tissue displays viscous effects and stress relaxation under constant deformation.**

Experiments have shown that porous effects may contribute significantly to the mechanical response of the brain tissue [22,58,59].

Nevertheless, most constitutive models for the brain tissue only consider the solid phase, i.e., they are monophasic, either purely elastic or viscoelastic. The deformation gradient  $\mathbf{F}$  is the only independent kinematic parameter in these monophasic models. Yet, monophasic models are still capable of describing the effects of other phases, e.g., by employing multiple time scales, see Sec. 5.3, or constitutive components, see Sec. 5.4. In fact, most monophasic models follow one of these approaches. Therefore, the notion of viscoelasticity might be slightly misleading. The capability of describing multiple phase effects and the conceptual simplicity explains why monophasic models are widely used for the brain tissue.

Biphasic and triphasic models are used when the effects of the other phases are non-negligible. These models have been used for the brain tissue to study hydrocephalus, an accumulation of cerebrospinal fluid in the ventricles of the brain [60,61]. Biphasic constitutive models are also used to explore mass- or drug-transport throughout the brain [62,63].

Biphasic models, often referred to as poroelastic models, include the fluid phase in addition to the solid phase. The state of the fluid phase is described by the fluid concentration  $c^f$  in analogy to the deformation gradient in the solid phase and the fluid pressure  $p$  in analogy to the elastic stress. The fluid phase introduces an additional independent parameter into the constitutive model [64]. The governing equations for poroelasticity are summarized as [65]

$$\begin{aligned} \nabla \cdot (\boldsymbol{\sigma}^s + \boldsymbol{\sigma}^f) &= 0 \\ \nabla \cdot \mathbf{q} &= 0 \\ \nabla \cdot \boldsymbol{\sigma}^f + \mathbf{R}^f &= 0 \end{aligned} \quad (61)$$

in which  $\boldsymbol{\sigma}^s$  and  $\boldsymbol{\sigma}^f$  are the solid and fluid stress, respectively,  $\mathbf{q}$  is the rate of fluid flow, and  $\mathbf{R}^f$  is the rate of linear momentum of the fluid. The fluid stress is fully determined by the fluid pressure  $p$  and the concentration  $c^f$  as  $\boldsymbol{\sigma}^f = p c^f \mathbf{I}$ . The biphasic constitutive model provides relations between solid stress and strain and between fluid concentration and pressure. Darcy's law is a special case of Eq. (61) for a linear, gradient-dependent flux  $\mathbf{R}^f$  [65].

Triphasic models for the brain tissue can explain the pathophysiology of hydrocephalus, an excess of water in the brain [61]. The additional third phase in this model represents the ionic concentrations. Another triphasic model with the same constituents has been proposed to couple brain tissue swelling to oxygen delivery

[66]. Similar to the biphasic model, additional governing equations are required to characterize the spatiotemporal evolution of this third phase. In many diseased states, the fluid phase and other phases play a critical role since their alterations might have a serious impact on the mechanical of brain tissue [5]. Yet, as most constitutive models for brain tissue are monophasic, we focus on these models in the remainder of this section.

**5.2 Complex Moduli Models.** A common experiment to characterize the linear viscoelastic response of a material consists of applying a sinusoidal shear displacement,  $\gamma = \gamma_0 \sin(\omega t)$ , and measuring the shear stress response,  $\tau = \tau_0 \sin(\omega t + \delta)$ . The shear lag is  $\delta = 0$  for a perfect elastic material and  $\delta = \pi/2$  for a perfect fluid. A convenient way to represent this response is by the complex shear modulus  $\mu^*$

$$\mu^* = \mu' + i \mu'' \quad \text{with} \quad \begin{aligned} \mu' &= \tau_0/\gamma_0 \cos(\delta) \\ \mu'' &= \tau_0/\gamma_0 \sin(\delta) \end{aligned} \quad (62)$$

in which  $\mu'$  and  $\mu''$  are the storage and loss shear moduli. The expression in Eq. (62) allows us to show that  $\mu'$  is a measure of the maximum amount of elastic energy stored in the material, and  $\mu''$  is a measure of the energy dissipation during a single sinusoidal load cycle. The complex shear modulus has been measured for brain tissue in the early days of testing [7], but was later abandoned upon recognizing the nonlinear nature of the brain tissue. With the advance of magnetic resonance elastography, linear viscoelasticity and the complex modulus are currently regaining popularity as diagnostic tools to understand the mechanisms of neurological disorders [39,41,67].

**5.3 Convolution Models.** Convolution modeling is the simplest and most commonly used method to describe the time-dependent behavior of brain tissue. The basic idea is to use time-dependent stiffness moduli and hence a time-dependent strain energy function. The convolution method is motivated by relaxation experiments that are often performed to characterize the viscoelastic properties of soft tissue. Indeed, in relaxation experiments, the applied deformation is held constant and the resistant force is measured over time. Time dependence can then be attributed to time-dependent stiffness moduli (30).

A widely used technique to describe the evolution of stiffness moduli in time is the Prony series approach [33,43–45,47–49]

$$\mu(t) = \mu_0 \left[ 1 - \sum_{k=1}^n g_k [1 - \exp(-t/\tau_k)] \right] \quad (63)$$

where  $\mu_0$  is the shear stiffness,  $g_k$  are the stiffness weights associated with the different time constants, and  $\tau_k$  are the characteristic time constants of the material. For linear viscoelasticity and in a relaxation-type loading, Prony series are equivalent to the generalized Maxwell model [68]. Most models use two time constant,  $n = 2$ , and rationalize this approach by attributing one time scale to the porous structure of brain tissue and one time scale to the viscous behavior. At infinite time, we obtain the steady-state modulus  $\mu_\infty$

$$\mu_\infty = \lim_{t \rightarrow \infty} (\mu(t)) = \mu_0 \left[ 1 - \sum_{k=1}^n g_k \right] \quad (64)$$

The model described here assumes that the time-dependent behavior is independent of the tissue deformation. Experiments suggest that this linear viscoelastic model is only valid for brain tissue up to strains on the order of 0.1% [6].

Table 2 summarizes the different time scales  $\tau_k$  reported in the literature. Interestingly, the observed time constants seem to depend significantly on the loading rates. Experiments at higher loading rates seem to suggest lower time scales  $\tau_k$  and vice versa.

**Table 2 Experimental values for time scales  $\tau_k$  reported in the literature**

	Time constants, $\tau_k$ (s)		Holding time (s)	Loading rate	Remarks
Mendis et al. [43]	$\tau_1 = 0.008$	$\tau_2 = 0.15$	0.1	0.25 (m/s)	Indentation experiments
Miller and Chinzei [44,47]	$\tau_1 = 0.5$	$\tau_2 = 50$	N/A	$0.64, 0.64 \times 10^{-2},$ and $0.64 \times 10^{-5}$ (1/s)	Time constants predetermined
Prange and Margulies [48]	$\tau_1 = 0.15 - 0.2$	$\tau_2 = 2.4 - 3.0$	100	0.42–8.33 (1/s)	—
Laksari et al. [33]	$\tau_1 = 0.01$	$\tau_2 = 1$	120–180	10 (1/s)	Time constants predetermined
	$\tau_3 = 10$	$\tau_4 = 100$			
Rashid et al. [49]	$\tau_1 = 0.011$	$\tau_2 = 0.0264$	0.14	30, 60, 90, and 120 (1/s)	—
Budday et al. [69]	$\tau_1 = 4.2$	$\tau_2 = 160$	600	$5 \times 10^{-6}$ (m/s)	Indentation experiments

This observation clearly demonstrates the dependence of the constitutive behavior of brain tissue on the loading rate and highlights the challenges associated with characterizing the response of ultrasoft poroviscoelastic materials.

Equation (63) is only valid for relaxation experiments with a constant applied deformation and a time-varying force. Due to the linear character of the model, the convolution integral can be used to generalize this model to any type of displacement-controlled loading. For example, for a Neo-Hookean material model (35), the convolution-type strain energy becomes

$$\Psi_{nh}(t) = \int_0^t \frac{1}{2} \mu(t - \tau) \frac{d}{d\tau} [I_1 - 3] d\tau \quad (65)$$

The convolution integral is closely related to the complex modulus for linear viscoelastic materials in Sec. 5.2. Indeed, applying the convolution integral with a sinusoidal deformation to a linear elastic material yields the relation between the complex modulus  $\mu^*$ , the time constants  $\tau_k$ , and loading frequency  $\omega$  [70].

For general loading cases, the convolution integral is often expensive to evaluate numerically. The high computational cost together with the linearity of the model are the two major limitations of convolution-type models. Especially, the linearity assumption seems rather restrictive since brain tissue, in its physiological regime, might easily undergo deformations beyond what has been reported as the linear limit of 0.1% strain.

**5.4 Multiplicative Decomposition Models.** A more general approach to model the time-dependent behavior of brain tissue is to decompose the deformation gradient into a time-independent elastic and a time-dependent viscous part. If necessary, these parts can then be subdivided further, which immediately indicates one of the advantages of this method: The constitutive model can be constructed from multiple building blocks that represent the key physical features of the tissue. In addition, by choosing an appropriate constitutive relation for each building block, the resulting model will be fully nonlinear and perfectly embedded in the realm of finite deformation continuum mechanics. Multiplicative decomposition models inherently account for the material response to large deformations and high strain rates, features that are essential to model high-impact loading, e.g., in traumatic brain injury [49].

Figure 4 illustrates the kinematics of the multiplicative decomposition of the deformation gradient into an elastic and a viscous part. This decomposition was first introduced for elastoplasticity [71], then used for viscoelasticity [72], and later applied to growth [73] and viscoplasticity [74]. In all the cases, the deformation gradient is decomposed into an elastic part and an inelastic part that represents the plastic, viscous, growth, or viscoplastic deformation. Within a finite element setting, the numerical solution of multiplicative decomposition models uses the concept of internal variables to keep track of the history of the inelastic deformation [75].

In this section, we first present a short discussion of the governing equations for the multiplicative decomposition method. We then show how it applies to the generalization of the standard linear solid model for viscoelasticity into a nonlinear, continuum

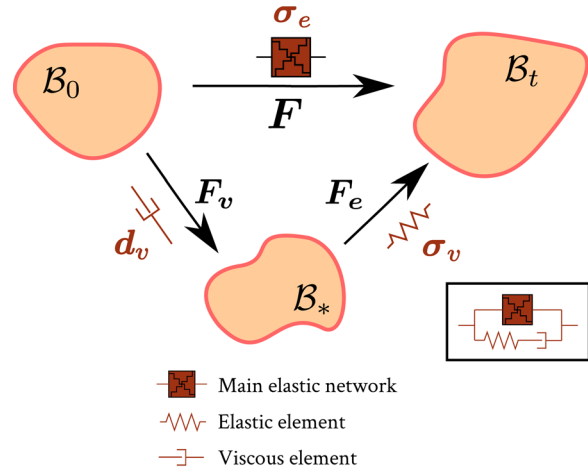


**Fig. 4 Multiplicative decomposition model and standard linear solid model. Every component of the deformation gradient is associated with a rheological element:  $F$ ,  $F_e$ , and  $F_v$  are related to the main elastic network, the elastic spring, and the viscous damper. These elements require individual constitutive relations to define the elastic stress  $\sigma_e$ , the viscous stress  $\sigma_v$ , and the viscous stretch rate  $d_v$ .**

mechanics setting. Finally, we highlight three constitutive models for brain tissue, which are based on the multiplicative decomposition approach [14–16].

The fundamental kinematic assumption of this approach is to multiplicatively decompose the deformation gradient into an elastic part  $F_e$  and a viscous part  $F_v$

$$F = F_e \cdot F_v \quad (66)$$

Both the elastic and viscous parts are functions of position  $X$  and time  $t$ . The viscous part of the deformation is dissipative and decays in time,  $\lim_{t \rightarrow \infty} (F_v(t)) = I$ . The multiplicative decomposition of the deformation gradient is typically combined with the additive decomposition of the free energy  $\Psi$  into an elastic and a viscous part [75]

$$\Psi = \Psi_\infty(C) + \Psi_v(C_e) \quad (67)$$

in which  $\Psi_\infty(C)$  represents the steady-state elastic strain energy, and  $\Psi_v(C_e)$  contains the time-dependent contribution to the total strain energy.  $C$  is the right Cauchy-Green deformation tensor as defined in Eq. (2), and  $C_e$  is its elastic counterpart,  $C_e = F_e^T \cdot F_e$ . The strain energy function in Eq. (67) defines the Cauchy stress  $\sigma$  according to Eq. (27) as

$$\sigma = -pI + \frac{2}{J} \left[ F \cdot \frac{\partial \Psi_\infty}{\partial C} \cdot F^T + F_v \cdot \frac{\partial \Psi_v}{\partial C_e} \cdot F_v^T \right] \quad (68)$$

The velocity gradient

$$l = \dot{F} \cdot F^{-1} = \dot{F}_e \cdot F_e^{-1} + F_e \cdot \dot{F}_v \cdot F_v^{-1} \cdot F_e^{-1} \quad (69)$$

is important in constitutive models for viscoelasticity, as it determines the dissipative behavior of the viscous contribution. We adopt the following definitions:  $\mathbf{l}_e = \dot{\mathbf{F}}_e \cdot \mathbf{F}_e^{-1}$ ,  $\tilde{\mathbf{l}}_v = \dot{\mathbf{F}}_v \cdot \mathbf{F}_v^{-1}$ , and  $\mathbf{l}_v = \mathbf{F}_e \cdot \tilde{\mathbf{l}}_v \cdot \mathbf{F}_e^{-1}$ , such that the total velocity gradient decomposes additively into an elastic and a viscous part. Note that  $\mathbf{l}_e$  and  $\mathbf{l}_v$  are both defined in the current configuration, and hence they are both purely Eulerian quantities

$$\mathbf{l} = \mathbf{l}_e + \mathbf{l}_v \quad \text{with} \quad \mathbf{l}_v = \mathbf{d}_v + \mathbf{w}_v \quad (70)$$

Similar to the total velocity gradient in Eq. (9), we can decompose the viscous rate of deformation into a symmetric part  $\mathbf{d}_v$  and a skew-symmetric part  $\mathbf{w}_v$ , which represent the viscous rate of stretch and viscous rate of spin. Almost all multiplicative decomposition models assume that the inelastic spin rate vanishes identically [14–16]

$$\mathbf{d}_v = \frac{1}{2} [\mathbf{l}_v + \mathbf{l}_v^T] = \mathbf{l}_v \quad \text{and} \quad \mathbf{w}_v = \frac{1}{2} [\mathbf{l}_v - \mathbf{l}_v^T] = \mathbf{0} \quad (71)$$

To close the set of equations, it remains to define a constitutive relation for the viscous stretch rate  $\mathbf{d}_v$ , or rather  $\mathbf{l}_v$ . The evolution for the viscous spin rate  $\mathbf{l}_v$  follows from the second law of thermodynamics [75]:

$$\frac{\partial \Psi_v}{\partial \mathbf{C}_e} : [\mathbf{C}_e \cdot \tilde{\mathbf{l}}_v] \geq 0 \quad \forall \mathbf{C}_e, \tilde{\mathbf{l}}_v \quad (72)$$

A definition that is consistent with this second law is to assume that the evolution of the viscous spin rate is driven by the viscous stress,  $\mathbf{d}_v = \mathbf{l}_v = f(\boldsymbol{\sigma}_v)$ .

Figure 4 illustrates how to generalize the standard linear solid model into the nonlinear continuum setting. The energy  $\Psi_\infty$  in Eq. (67) is associated with the overall deformation  $\mathbf{F}$  acting on the main elastic network of brain fibers; the energy  $\Psi_v$  in Eq. (67) is associated with the elastic, reversible part of the deformation  $\mathbf{F}_e$ ; and the evolution equation for  $\mathbf{d}_v$  is associated with the viscous component of the deformation  $\mathbf{F}_v$ . The main elastic network is a special elastic element, as it is generally governed by a more complex constitutive relation [14–16].

Figure 4 can be interpreted as a rheological model composed of parallel and serial building blocks of springs and dampers. Using this idea, more advanced constitutive models can be constructed by modifying or adding building blocks. The former is achieved by modifying the constitutive relation of the individual components, and the latter by adding more intermediate configurations with corresponding constitutive relations. Three popular constitutive models for brain tissue that can be constructed by using this concept: the Hrapko model [15], the Bilston model [14], and the Prevost model [16].

**5.4.1 Hrapko Model.** The Hrapko model is a popular model for brain tissue [15]. It is conceptually similar to the generic model in Fig. 4, but with multiple parallel configurations  $\mathcal{B}_*^k$ ,  $k = 1, \dots, n$ .

Figure 5 illustrates the interpretation of the Hrapko model as the continuum version of the generalized Maxwell model. The model parameter  $n$  is closely related to the number of time scales in the convolution method (63). Accordingly, the Hrapko strain energy function is very similar to Eq. (67)

$$\Psi^{\text{hr}} = \Psi_\infty(\mathbf{C}) + \sum_{k=1}^n \Psi_v^k(\mathbf{C}_e^k) \quad (73)$$

Figure 5 indicates that the Hrapko model requires  $1 + 2n$  individual constitutive relations, i.e., one for each parameter denoted next to each rheological symbol. The stress in the brain fiber network,  $\boldsymbol{\sigma}_e$ , is determined by Eq. (57) and the  $k = 1, \dots, n$  stresses in the parallel networks,  $\boldsymbol{\sigma}_v^k$ , by Eq. (56). The viscous stretch rates,

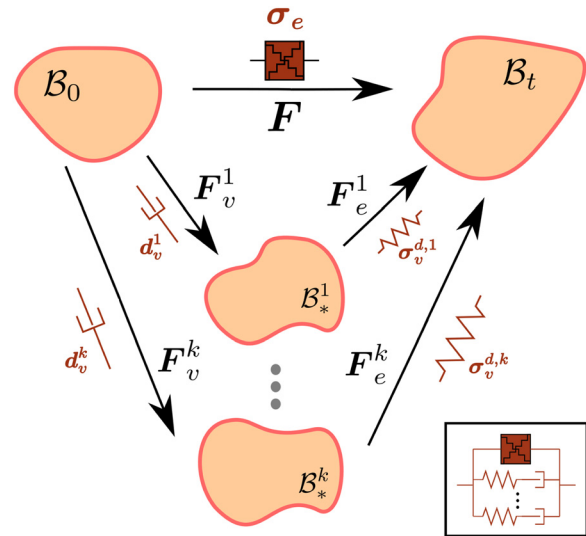


**Fig. 5 Hrapko model [15] and Bilston model [14] as examples of multiplicative decomposition models. Both models are popular viscoelastic models for the brain tissue based on multiple parallel configurations.**

$\mathbf{d}_v^{\text{hr},k}$ , depend on the deviatoric part of the viscous stresses,  $\boldsymbol{\sigma}_v^{d,k}$ , in analogy to a nonlinear damper element

$$\mathbf{d}_v^{\text{hr},k} = \frac{1}{2\eta^{\text{hr},k}} \boldsymbol{\sigma}_v^{d,k} \quad (74)$$

in which  $\eta^{\text{hr},k}$  denotes the viscosity of the brain tissue. The viscosity is a function of the invariant stress measure  $\tau = \sqrt{(1/2)\boldsymbol{\sigma}^d : \boldsymbol{\sigma}^d}$ , with  $\boldsymbol{\sigma}^d = \boldsymbol{\sigma}_e^d + \sum_{k=1}^n \boldsymbol{\sigma}_v^{d,k}$ , by the Ellis model [76]. The Ellis model is a phenomenological relationship between the viscosity  $\eta$  and the stress measure  $\tau$  for a non-Newtonian flow in a porous medium [76]

$$\eta^{\text{hr},k}(\tau) = \eta_\infty^k + \frac{\eta_0^k - \eta_\infty^k}{1 + [\tau/\tau_0]^{n-1}} \quad (75)$$

The combination of Eqs. (56), (57), and (74) yields all  $1 + 2n$  individual constitutive relations to close the set of equations of the Hrapko model. If all the rheological elements in the Hrapko model were linear, it would reduce to the generalized Maxwell model, which is equivalent to the Prony series in a classical relaxation experiment (63).

**5.4.2 The Bilston Model.** The Bilston model [14] is very similar to the Hrapko model as it consists of exactly the same configuration of constitutive elements illustrated in Fig. 5. Yet, the constitutive equations that govern the individual components in the Bilston model are different from the Hrapko model. The elastic stress in the brain fiber network,  $\boldsymbol{\sigma}_e$ , follows from the strain energy function in Eq. (58). The stresses in the parallel networks are not determined by a strain energy function; instead, the relation between stress and stress rate in each parallel network is prescribed. The main difference between the Bilston model and the Hrapko model is that the stress in each parallel network depends on the total stretch rate  $\mathbf{d}$ , rather than on the stretch rate in the parallel network  $\mathbf{d}_v^k$

$$\mathbf{d}^{\text{bil}} = \frac{1}{2\eta^{\text{bil},k}} \left[ \boldsymbol{\sigma}_v^k + \lambda^k \left[ \frac{d\boldsymbol{\sigma}_v^k}{dt} - \nabla \mathbf{v}^T \cdot \boldsymbol{\sigma}_v^k - \boldsymbol{\sigma}_v^k \cdot \nabla \mathbf{v} \right] \right] \quad (76)$$

For displacement-controlled loading,  $\mathbf{d}$  is known, and Eq. (76) can be solved for the stresses in each network. The viscosity  $\eta^{\text{bil},k}$  is a function of  $J_2$ , the second invariant of  $\mathbf{d}$ , according to the Carreau shear-rate model [77]

$$\eta^{\text{bil},k}(J_2) = \eta_\infty^k + \frac{\eta_0^k - \eta_\infty^k}{[1 - 2\tau^2 J_2]^{(n-1)/2}} \quad (77)$$

where  $\eta_0^k$  and  $\eta_\infty^k$  are the parameters similar to the Hrapko model, and  $\tau$  is a material parameter that represents the shear rate at which shear thinning begins. The function  $\lambda^k(I_1, I_2) = \lambda^{\text{lv},k}[1 + k(x - x^{\text{lv}})]$  describes the relaxation characteristics of each parallel network, in which  $x(I_1, I_2) = \sqrt{aI_1 + [1 - a]I_2 - 3}$  weights the influence of the first and second invariants as in Eq. (58), and  $k$ ,  $\lambda^{\text{lv},k}$ , and  $x^{\text{lv}}$  are the material constants. The viscosity  $\eta^{\text{bil},k}$  and relaxation parameter  $\lambda^k$  in the Bilston model are related by the shear modulus of the parallel network as  $\eta^{\text{bil},k} = \mu^k \lambda^k$ . The familiar storage and loss moduli are obtained analytically from  $\lambda^k$  and  $\mu^k$  as functions of the loading frequency [70]. Finally, the total stress in the Bilston model is  $\sigma = -p\mathbf{I} + \sigma_e + [[C_1 x]^{p_1} + 1]^{(m-1)/2} \exp(-C_2 x^{p_2}) \sum_{k=1}^n \sigma_v^k$ , with  $x(I_1, I_2)$  as in Eq. (58).

**5.4.3 The Prevost Model.** The third constitutive brain model that can be constructed from Fig. 4 is the Prevost model illustrated in Fig. 6. The individual components of the Prevost model are more physics-based, but the arrangement of the different components is still phenomenological in nature [16]. The stress in the main elastic network  $\sigma_A$  is determined by a freely jointed eight-chain model, see Eqs. (59) and (60). The short- and long-term responses of the tissue are determined by other elastic networks, as  $\sigma_C$  and  $\sigma_E$ , respectively. The stresses  $\sigma_B$  and  $\sigma_D$  simply follow from equilibrium conditions  $\sigma_B = \sigma_A - \sigma_C$  and  $\sigma_D = \sigma_C - \sigma_E$ . The viscous stretch rate in the main viscous component  $d_B$  is based on the Bergström-Boyce model for elastomers and soft biological tissues [78]

$$d_B^{\text{prv}} = \dot{\gamma}_B \cdot \tilde{N}_B \quad (78)$$

in which  $\dot{\gamma}$  is a scaling parameter based on a nonlinear scaling law for polymers, which is assumed to be constant for brain tissue [16].  $\tilde{N}_B = \sigma_B / \|\sigma_B\|_F$  represents the direction of the driving stress  $\sigma_B$ , where  $\|\cdot\|_F$  denotes the Frobenius norm. Note that  $d_B$  is defined in the current configuration  $\mathcal{B}_t$ . The rate of viscous stretch in the second viscous component is similar to Eq. (74)

$$d_D^{\text{prv}} = \frac{1}{\sqrt{2}\eta} S_D \quad (79)$$

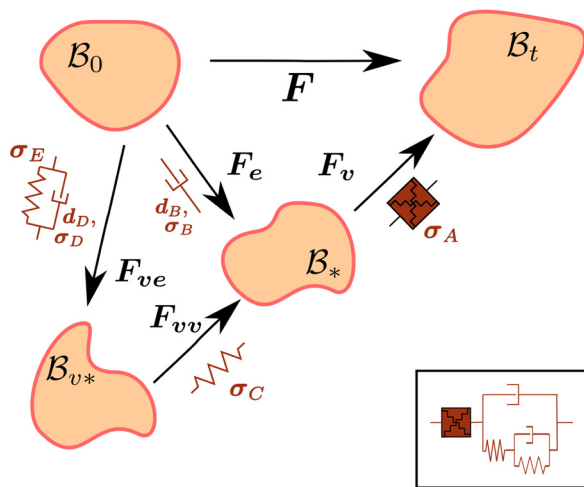


**Fig. 6** Prevost model [16] as example of multiplicative decomposition model. The Prevost model is a popular viscoelastic model for the brain tissue based on four configurations.

in which the viscosity  $\eta$  is assumed to be a constant, and  $S_D$  is a stress measure of  $\sigma_D$  in the relaxed configuration  $\mathcal{B}_*$ . As a result, also  $d_D$  is defined in  $\mathcal{B}_*$ .

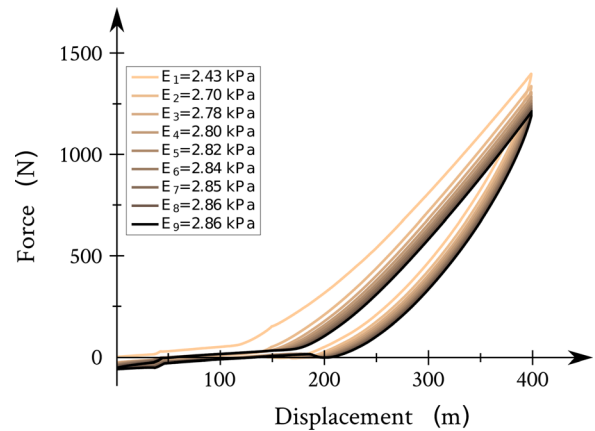
In Sec. 7, we will discuss the similarities and differences between the Hrapko, Bilston, and Prevost models in detail.

## 6 History-Dependent Modeling of Brain Tissue

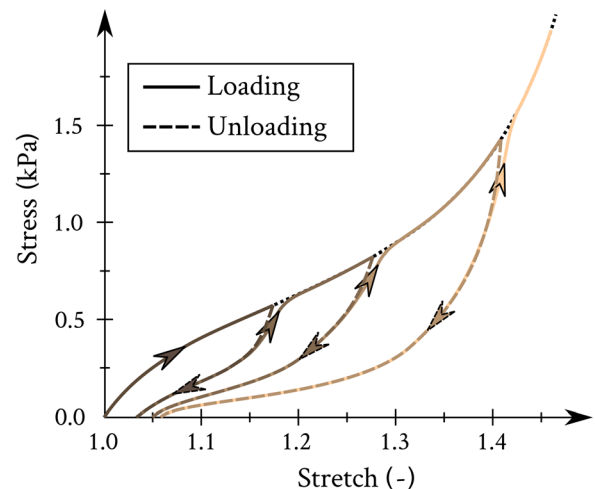
Various experiments have shown that preconditioning has a significant effect on the mechanical properties of brain tissue [9,22], which implies that the tissue response depends critically on the loading history.

Figure 7 illustrates our experimentally measured history-dependence, which agrees with the common rule of thumb that the constitutive response of brain tissue converges after approximately seven preconditioning cycles [6]. The effect of preconditioning is characteristic for rubberlike materials and polymers, where it is typically associated with the Mullins effect [79]. The Mullins effect represents a stress-softening of the material that depends on the maximum strain experienced during the loading history [80]. This phenomenon is often accompanied by residual strains after several loading–unloading cycles.

Figure 8 illustrates the characteristic stress–stretch behavior for the Mullins effect and residual strains under uniaxial



**Fig. 7** History-dependent response of the brain tissue under uniaxial loading–unloading. The brain tissue displays a preconditioning effect that converges after approximately seven preconditioning cycles.



**Fig. 8** History-dependent response under uniaxial loading–unloading displaying the Mullins effect and residual strains similar to rubberlike materials

loading–unloading. Each loading curve follows the unloading curve of the previous cycle up to the maximum experienced strain, after which it proceeds along the initial stress–strain curve. After unloading to a stress-free state, residual strains reside in the tissue.

Although conceptually similar, the Mullins effect is not identical to continuum damage because it recovers with time. It is the same for different load cases, and failure is not directly related to the Mullins effect [81]. Nevertheless, the Mullins effect can be modeled by a continuum damage mechanics approach [82]. Continuum damage models adopt a modified strain energy function

$$\Psi(\mathbf{C}, d) = [1 - d] \Psi_0(\mathbf{C}) \quad (80)$$

in which  $d$  is a damage parameter that depends on the strain history of the material, and  $\Psi_0$  is the strain energy function of the undamaged brain tissue. In the initial state, the damage parameter is zero,  $d = 0$ , and it increases,  $0 \leq d \leq 1$ , as damage accumulates within the material. While Eq. (80) accounts for damage-induced stiffness degradation, it does not account for the residual strains.

**6.1 Franceschini Model.** The Franceschini model is a constitutive model for brain tissue that incorporates both the Mullins effect and residual strains [22]. It is based on a modified Dorfmann strain energy function [83]

$$\Psi^{\text{fra}} = \eta_1 \Psi_0(\mathbf{C}) + (1 - \eta_2) \tilde{\Psi}(\mathbf{C}) + \phi_1(\eta_1) + \phi_2(\eta_2) \quad (81)$$

in which  $\eta_1$  and  $\phi_1(\eta_1)$  represent the perfect Mullins effect, and  $\eta_2$  and  $\phi_2(\eta_2)$  are the residual strains.  $\Psi_0(\mathbf{C})$  is the Ogden strain energy function (30), and  $\tilde{\Psi}(\mathbf{C})$  is a modified Neo-Hookean strain energy function that characterizes the residual strains. In this setup,  $\eta_1$  takes a similar interpretation as the damage weighting factor,  $[1 - d]$ , in Eq. (80). For the special case of uniaxial, incompressible deformation [22], the right Cauchy-Green tensor  $\mathbf{C}$  is fully determined by the stretch  $\lambda$ , see Eq. (19). For this special case, the parameter  $\eta_1$  follows as:

$$\eta_1^{\text{fra}}(\lambda) = 1 - \frac{1}{r} \tanh\left(\frac{\Psi_0(\lambda^{\text{max}}) - \Psi_0(\lambda)}{\mu m}\right) \quad (82)$$

where  $\lambda_{\text{max}}$  is the maximum stretch within the loading history,  $\mu$  is the shear modulus, and  $r$  and  $m$  are the additional material parameters. The Franceschini model is able to accurately fit experimental loading–unloading cycles, but not the change from tension into compression loading and vice versa [22]. To address this deficiency, a recent model combined a viscoelastic and an elastoplastic approach [84] to reproduce the experimentally observed behavior under cyclic loading [22] more accurately.

## 7 Discussion

The importance of mechanical forces, stress, and strain in understanding the form and function of our brain is increasingly recognized, not only among basic scientists [5]. In this review, we have revisited the different aspects of constitutive models for the brain tissue. Specifically, in Secs. 4–6, we have summarized widely used concepts to characterize the time-independent, time-dependent, and history-dependent behavior of the brain tissue.

Table 3 provides a systematic overview of how these individual time-independent, time-dependent, and history-dependent approaches have been combined into state-of-the-art models for the brain tissue. The last column of Table 3 summarizes the number of material parameters of each model. To some extent, this number is an indicator for the complexity of the model, or rather, for the complexity of the necessary parameter calibration. This summary does not include the predetermined parameters, e.g., predetermined time scales [33,44,47], as independently listed parameters. In the remainder of this section, we will discuss the constitutive modeling of the brain tissue with a particular

emphasis on the models summarized in Table 3. We will consider *physical motivation* and *practical relevance* as two important criteria to evaluate and compare the different approaches.

**7.1 Relevant Parameters for Brain Tissue Behavior.** The experimental characterization of the mechanical properties of the brain tissue has been an active field of research for more than half a century [7,35,86]. However, the scatter in the available experimental data is enormous with reported stiffness moduli covering multiple orders of magnitude from 0.1 kPa to 10 kPa. It is critically important to understand the relevant parameters that lead to this large scatter in the experimental data, both to acquire more consistent experimental data and to develop constitutive models for the brain tissue. In a recent comprehensive overview, parameter discrepancies are attributed to different testing methods, equipment, specimen size, loading rate, preconditioning, age, species, regional and directional variations, and in vitro versus in vivo testing [9]. A quantitative assessment of these effects is difficult to obtain, apart from loading rate and preconditioning. Some quantifications have been reported for the effects of age [42], species [48], and regional variations [69,87].

Not all parameters that affect the experimental data can be considered via constitutive modeling. In fact, the effects of the testing method, equipment, and specimen size are not intrinsic to the tissue properties. Therefore, they should not affect the constitutive model, but rather the geometry and boundary conditions.

For the remaining relevant parameters, it is important to know whether their effects are simply quantitative, or also qualitative. The loading rate, for example, has a direct qualitative effect: it can change the rheology from time-independent to time-dependent. Besides the loading rate, only preconditioning has been shown experimentally to have a qualitative effect: it can change the rheology from strain-softening to strain-hardening after the first loading cycle [22]. Other parameters, such as species, regional, directional, and age-dependent variations [48], and in vitro versus in vivo testing [88], are generally assumed to have mainly a quantitative effect: they do not change the rheology, but rather affect the range of the material parameters of interest. For example, in vivo studies of the human brain reported shear stiffnesses of 2.7 kPa and 2.4 kPa for white and 3.1 kPa and 2.3 kPa for gray matter tissue using magnetic resonance elastography [39,89]. These values naturally increase with increasing frequency, e.g., from 3 kPa at 400 Hz to 7 kPa at 800 Hz in the ferret brain [20]. In comparison, the ex vivo stiffness of bovine brain was reported to be 1.9 kPa for white and 1.4 kPa for gray matter tissue using nanoindentation [69]. While the in vivo and ex vivo stiffnesses of many soft tissues including cardiac muscle [90] or heart valves [13] may vary by up to 3 orders of magnitude and more, these studies suggest that for the brain, the in vivo stiffness is marginally larger than the ex vivo stiffnesses, yet of the same order of magnitude.

The nature of the relevant parameters explains why, to date, only the loading rate effect, the time-dependency, has been explicitly incorporated into brain tissue models. Although preconditioning is increasingly recognized to have a qualitative effect, it has not been explicitly incorporated yet, mainly because its effect still remains poorly understood. Therefore, all the material parameters for the brain tissue in Table 3 either describe the time-independent behavior, e.g., through stiffness moduli, or the time-independent behavior, e.g., through time constants. All other, purely qualitative effects are represented implicitly, e.g., through modifying the values of the material parameters.

**7.2 Physical Motivation of Constitutive Models.** Most of the commonly used constitutive models for brain tissue are purely phenomenological, a few models are microstructurally motivated, but none of the models is entirely physics-based. For example, the time-independent material response of the brain tissue in Sec. 4 is typically described by one of the phenomenological baseline

**Table 3 Overview of the constitutive models for the brain tissue reported in the literature**

	Time-independent	Time-dependent	Additional remarks	Loading case	Parameters
Pamidi and Advani [51]	Neo-Hookean, see Eq. (35)	—	Power function instead of strain energy function	Uniaxial compression	3
Mendis et al. [43] and Miller and Chinzei [44]	Polynomial with $N = 2$ , see Eq. (41)	Convolution with $n = 2$ , see Sec. 5.3	Time constants for convolution are pre-determined in Ref. [44]	Uniaxial compression	6
Bilston et al. [14]	Mooney–Rivlin with damping, see Eq. (58)	Upper convected Maxwell model [77], which is a special case of deformation split, see Sec. 5.4	—	Shear relaxation and constant shear-rate experiments	20
Miller and Chinzei [47] and Prange and Margulies [48]	Ogden with $N = 1$ , see Eq. (30)	Convolution with $n = 2$ , see Sec. 5.3	Time constants for convolution are pre-determined in Ref. [47]	Uniaxial tension [47] and shear relaxation [48]	4
Franceschini et al. [22]	Ogden with $N = 2$ , see Eq. (30)	Terzaghi consolidation theory [85]	Mullins effect and residual strains are considered, see Sec. 6	Cyclic uniaxial tension/compression	8
Hrapko et al. [15]	Combination of Mooney–Rivlin and Neo-Hookean, see Eq. (56) and combination of exponential and quadratic, see Eq. (57)	Deformation split, see Eq. (73) and Fig. 5	This model can be understood as the continuum version of the generalized Maxwell model	Shear relaxation and constant shear-rate experiments	16
Cloots et al. [32]	Compressible Holzapfel model with Neo-Hookean model as isotropic contribution, see after Eqs. (47), (35), and (53)	—	Theoretical study	—	3
Prevost et al. [16]	Compressible eight-chain model for macromolecular elastic networks, see Eqs. (59) and (60)	Deformation split, see Eqs. (78) and (79) and Fig. 6	—	Indentation	8
Laksari et al. [33]	Compressible polynomial, see Eqs. (41) and (52)	Convolution with $n = 4$ , see Sec. 5.3	Time constants for convolution are predetermined	Uniaxial compression	10
Rashid et al. [49]	Ogden with $N = 1$ , see Eq. (30)	Convolution with $n = 2$ , see Sec. 5.3	Ogden model performed better than Fung, Gent, and Mooney–Rivlin models	Shear	5

models in Sec. 3.2. Similarly, the time-dependent response in Sec. 5 is commonly represented by phenomenological convolution methods in Sec. 5.3 or by a phenomenological arrangement of rheological building blocks in the multiplicative decomposition method in Sec. 5.4. Nevertheless, it is often possible to relate the material parameters of a phenomenological model to a physical event. We consider the ability of attributing a physical meaning to each material parameter in a model as a measure for the physical motivation.

Modeling the time-independent response of the brain tissue is typically achieved by the Ogden model or one of its special cases, the Mooney–Rivlin or the Neo-Hookean model [14,15,22,32,47–51]. The Ogden model (30) consists of material parameters  $\alpha_i$ ,  $\mu_i$ , and  $N$ . For the Mooney–Rivlin model (33) with  $\alpha_1 = 2$  and  $\alpha_2 = -2$ , we can interpret the values for  $\mu_1$  and  $\mu_2$  as the stiffness parameters for the first two deformation modes,  $I_1$  and  $I_2$ . For the Neo-Hookean model (35) with  $\alpha_1 = 2$ ,  $\mu$  is the stiffness parameter associated with a single deformation mode,  $I_1$ . For general values for  $\alpha_i$ , there is no correlation between the parameters  $\mu_i$  and individual deformation modes. Nonetheless, the  $\alpha_i$  have a well-defined physical interpretation as they allow to distinguish between stress-softening behavior, for  $|\alpha_i| \leq 1$  for all  $i = 1, \dots, N$ , and stress-hardening behavior otherwise, see Fig. 2.

They also allow to characterize different behaviors in tension and compression [47]. This implies that  $\alpha_i$  can also be related to physical events. When combining these observations, we argue that the Ogden model with  $N = 2$  is physically well motivated. However, the sensitivity of the Ogden model to the value of  $\alpha_i$  is relatively small. As a result, the experimental values for  $\alpha_i$  span more than 3 orders of magnitude, see Table 1.

The polynomial model (41) is arguably less well-motivated than the Ogden model. Although it includes more material parameters, it is more restrictive because it neither allows to distinguish between softening and hardening nor between tension and compression.

Modeling the time-dependent response of the brain tissue introduces additional material parameters. The convolution model (63) in Sec. 5.3 requires  $2n$  additional parameters, where  $n$  is the number of time scales. The  $2n$  material parameters are the  $k = 1 \dots n$  characteristic time scales  $\tau_k$  and the associated stiffness fractions  $g_k$ . In a physically motivated, mechanistic constitutive model, each time scale should correspond to a physical effect. A common approach is to introduce two time scales,  $n = 2$ , associated with the viscous and porous responses of the tissue [43,44,47,49]. In some reports, the time scales  $\tau_k$  are predefined [33,44,47], which reduces the number of material parameters to  $n$ . However,

predefining the characteristic time scales puts an unnecessary restriction to the model, as these time scales should follow naturally from the experimental measurements.

A similar reasoning applies to the deformation split method in Sec. 5.4, where each constitutive component represents a different physical phenomenon. As typical examples of this approach, we highlighted the Hrapko model [15], the Bilston model [14], and the Prevost model [16] in Sec. 5.4. The individual components in the Prevost model (78) and (79) are attributed to individual physical events, whereas the large number of parallel components,  $n = 5$  in the Hrapko model (74) and  $n = 9$  in the Bilston model (76), makes the latter two models less well motivated. This number of parallel components is conceptually similar to the number of time scales in the convolution method, and the rheological building blocks of these multiplicative decomposition models contain a similar degree of physical motivation. For the main elastic network, the Hrapko and Bilston models adopt a model for polymers and the Prevost model uses the eight-chain network model. For the main viscous component, the Prevost model uses a physically motivated approach, whereas all other viscous components in all the three models are purely phenomenological. The Prevost model assumes a constant viscosity in these components, whereas the Hrapko and Bilston models adopt a stress and stretch rate dependent viscosity, which allows to model additional physical effects. Apart from different numbers of parallel components,  $n = 5$  in the Hrapko model and  $n = 9$  in the Bilston model, the Prevost, Hrapko, and Bilston models have a conceptually similar degree of physical motivation.

Modeling history-dependent effects introduces yet another level of complexity. As a typical example of a history-dependent model, the Franceschini model [22] in Sec. 6 captures the Mullins effect and the effect of residual strains. It introduces two additional material parameters to quantify these effects. The elastic strain energy function of the Franceschini model (80) adopts an Ogden-type approach, which has a similar physical motivation as discussed earlier in this section.

In general, we would expect that the number of model parameters reflects the extent by which the constitutive model captures the underlying physics. This trend can indeed be observed from Table 3. In this sense, the Bilston model [14], the Hrapko model [15], and the Laksari model [33] represent outliers with more material parameters. These outliers are constitutively expensive because they introduce a large number of characteristic time scales to accurately capture the time-dependent response of the brain tissue. These observations suggest to be cautious when using higher order models, which are known to have a tendency to overfit the data.

**7.3 Choosing a Constitutive Model.** The choice of a particular constitutive model for the brain tissue is very much determined by the driving physiological problem. The first consideration is to decide whether or not a multiphase model instead of a monophasic model is needed to capture the underlying phenomena. This is the case when the response of other phases than the solid phase is non-negligible, e.g., when studying fluid flow, drug, or oxygen transport, or simple local phenomena including swelling and edema. Multiphase models are usually intended to study the behavior of the additional phases and their interaction with the solid phase. If this is the case, the mechanical loading to the solid phase is usually small, and the detailed response of the solid phase may be of minor importance. The elastic response could be modeled by one of the baseline models in Sec. 3.2 or by one of the main elastic networks in the Hrapko, Bilston, or Prevost models in Sec. 5.4. In most reported multiphase models for the brain tissue in the literature, the constitutive model for the solid phase is time-independent and relatively simple, e.g., compressible Ogden [62], Neo-Hookean [66], or even linear elastic [60,61,63]. As a general rule of thumb, to model the time-dependent behavior in a multiphase problem, the constitutive model for the solid phase should have a limited number of time scales, arguably at most one.

This time scale should be attributed to the viscous response that is intrinsic to the solid phase itself. The time scales introduced by all other phases should follow naturally from their own governing equations or constitutive equations, not from the constitutive model of the solid phase. Of course, there could be additional time scales to capture the effects of phases that are not explicitly represented in the multiphase model. For example, an electrochemical time scale can be added if the multiphase model only considers the solid and fluid phases and if this time scale is relevant to the overall tissue physiology.

The choice of constitutive model depends largely on the physiological phenomenon of interest—not only for multiphase but also for monophasic models. It is critical to decide whether or not time-dependent effects play an important role. When studying extremely slow phenomena, e.g., neurodevelopment [91–93], it is likely sufficient to consider the steady-state, relaxed material response. The steady-state response is, by definition, time-independent, and a time-independent model seems sufficient to capture its effects. When studying fast phenomena associated with moderate to high loading rates, e.g., neurosurgery or traumatic brain injury [32], it becomes important to consider the transient material response.

Some general considerations should be considered when choosing a constitutive model for brain tissue: First, most constitutive models have only been validated by the experimental data of one specific load case, e.g., uniaxial tension, compression, or shear. A constitutive model that has been calibrated under similar loading conditions as the problem at hand is more credible than a model calibrated under different loading conditions. Similarly, the focus with which the experimental data have been collected should be aligned with the focus of the current study. For example, the Hrapko, Bilston, and Prevost models in Sec. 5.4 adopt a similar approach to model the response of brain tissue. However, the experimental focus was entirely different: The Hrapko and Bilston models characterize the response during large deformations; the Prevost model characterizes the response during loading, unloading, and relaxation [16].

Second, experimental evidence suggests that preconditioning of the tissue changes the material response in tension from stress softening into stress hardening [22]. Depending on the presence or absence of preconditioning, the preconditioning level, and the number of preconditioning cycles, the selected model should account for, or rather correct for, the effects of preconditioning.

Finally, and perhaps most importantly, it is critical to investigate how relevant the accuracy of the constitutive model is to the specific problem. For example, a particular study may investigate general trends, rather than specific details. If these trends are insensitive to the constitutive model, a highly accurate constitutive model might be unnecessarily expensive. Additionally, the strength of any model is determined by its weakest link. Depending on the application, this weakest link can be the wide scatter in experimental data for the brain tissue [11], the numerical representation of the highly complex brain geometry [94], or the boundary conditions at the brain–skull interface [95]. It may, therefore, be unnecessary to utilize a highly accurate constitutive model if other constituents of the numerical model are less well known. In these cases of lower required accuracy, it is wise to choose a simple, but sufficiently accurate constitutive model that entails low numerical costs. In a comparison of four different simple baseline constitutive models, the Ogden model, with  $\alpha_1 = 2.5$ – $4.8$  as in Table 1, yielded the best fit of experimental data [49]. Combined with its good physical motivation, see Sec. 7.2, the Ogden model seems to be an appropriate simple constitutive model. For higher accuracy, a constitutive model with a higher level physical motivation that captures all the relevant phenomena could be preferable, as discussed in Sec. 7.2. In any case, it is always important to question whether including additional parameters is truly necessary to increase the accuracy and physical motivation of the model or whether it unnecessarily increases model complexity.

**7.4 Perspectives.** In Sec. 7.3, we discussed that the Ogden model is often claimed to be an appropriate choice to model the elastic behavior for brain tissue. Besides this recommendation, there is little consensus on the constitutive modeling of the brain tissue in the literature. In this section, we outline some of the challenges and perspectives and suggest directions for future research.

First, in addition to the recommendation for a simple model of the time-independent response, it would also be useful to investigate a simple model to characterize the time-dependent response of the brain tissue. We presented several approaches to model the transient behavior of the brain tissue in Sec. 5; however, at the current stage, none of these models is entirely satisfactory. The convolution method in Sec. 5.3 is simple and relatively well established to describe relaxation experiments, but it is inherently linear and unattractive for general load cases. The multiplicative decomposition method in Sec. 5.4 can capture finite deformations, but it is relatively complex, and none of the discussed models has been broadly adopted by many other groups. Combining the advantages of both methods, it would be desirable to establish a constitutive model that is conceptually similar to the Hrapko model [15] or Bilston model [14] in Sec. 5.4, but uses only  $n = 2$  parallel configurations with simpler rheological building blocks. Ideally, the main elastic component would be an Ogden-type model and the viscous components simple nonlinear dampers (79).

Second, we recommend to consider several important aspects when designing more complex, physics-based constitutive models for the brain tissue. The development of more mechanistic models relies heavily on accurate and consistent experimental data [96]. These experimental data should be acquired and documented consistently across research groups as recommended by the recent guidelines [9]. A consistent documentation would be desirable for constitutive modeling as well. The documentation for a constitutive model should include the methods used for time-dependent and time-independent modeling, the experimental load case used to calibrate the model, the physiological phenomenon that the model was designed for, the physical interpretation of each material parameter, and the total number of material parameters, similar to Table 3. A common observation among existing constitutive models is that most models have been formulated in a general continuum mechanics setting, while their material parameters are typically fitted to a single experimental load case. Understandingly, the experimental challenges and high costs do often not allow for testing multiple load cases by one research group alone. The experimental validation may, however, be possible across research groups when experiments and constitutive models are consistent and well-documented.

Finally, understanding the relevant physics, physiology, and pathology of brain tissue at the molecular and cellular levels is essential for designing appropriate constitutive models at the tissue level [11]. Ideally, this understanding will not just generate purely phenomenological models to reproduce existing experimental curves, but mechanistic models to predict the behavior under physiological and pathological conditions [10]. Knowledge from the smaller scales will help us to understand which phenomena contribute to the brain tissue stiffness in the healthy state and to stiffness degradation in the diseased state [42]. It will also allow us to appreciate the rheological differences between gray and white matter tissue, to interpret the interfacial behavior at the cortical–subcortical transition [52]. With this understanding, it will be easier to correlate ex vivo measurements to in vivo behavior, a connection that is exceptionally difficult for ultrasoft materials like the brain [88]. Calibrated and validated constitutive models for the brain are a critical step toward explaining—and possibly even modulating—the response of the brain to environmental changes, for example, during high-impact loading or surgical intervention.

## References

[1] Chatelin, S., Constantinesco, A., and Willinger, R., 2010, “Fifty Years of Brain Tissue Mechanical Testing: From In Vitro to In Vivo Investigations,” *Biorheology*, **47**(5–6), pp. 255–276.

[2] Holbourn, A. H. S., 1943, “Mechanics of Head Injury,” *Lancet*, **242**(6267), pp. 438–441.

[3] Miller, K., 2011, *Biomechanics of the Brain*, Springer, New York.

[4] Bilston, L. E., 2011, *Neural Tissue Biomechanics*, Springer, Heidelberg, Germany.

[5] Goriely, A., Geers, M. G. D., Holzapfel, G. A., Jayamohan, J., Jérusalem, A., Sivaloganathan, S., Squier, W., van Dommelen, J. A. W., Waters, S., and Kuhl, E., 2015, “Mechanics of the Brain: Perspectives, Challenges, and Opportunities,” *Biomech. Model. Mechanobiol.*, **14**(5), pp. 931–965.

[6] Bilston, L. E., Liu, Z., and Phan-Thien, N., 1997, “Linear Viscoelastic Properties of Bovine Brain Tissue in Shear,” *Biorheology*, **34**(6), pp. 377–385.

[7] Fallenstein, G. T., Hulce, V. D., and Melvin, J. W., 1969, “Dynamic Mechanical Properties of Human Brain Tissue,” *J. Biomech.*, **2**(3), pp. 217–226.

[8] Holzapfel, G. A., 2000, *Nonlinear Solid Mechanics: A Continuum Approach for Engineering*, Wiley, Chichester, UK.

[9] Cheng, S., Clarke, E. C., and Bilston, L. E., 2008, “Rheological Properties of the Tissues of the Central Nervous System: A Review,” *Med. Eng. Phys.*, **30**(10), pp. 1318–1337.

[10] Goriely, A., Budday, S., and Kuhl, E., 2015, “Neuromechanics: From Neurons to Brain,” *Adv. Appl. Mech.*, **48**, pp. 79–139.

[11] Franze, K., Janmey, P. A., and Guck, J., 2013, “Mechanics in Neuronal Development and Repair,” *Annu. Rev. Biomed. Eng.*, **15**(1), pp. 227–251.

[12] Rausch, M. K., and E. K., 2013, “On the Effect of Prestrain and Residual Stress in Thin Biological Membranes,” *J. Mech. Phys. Solids*, **61**(9), pp. 1955–1969.

[13] Rausch, M. K., Famaey, N., O’Brien Shultz, T., Bothe, W., Miller, D. C., and Kuhl, E., 2013, “Mechanics of the Mitral Valve: A Critical Review, an In Vivo Parameter Identification, and the Effect of Prestrain,” *Biomech. Model. Mechanobiol.*, **12**(5), pp. 1053–1071.

[14] Bilston, L. E., Liu, Z., and Phan-Thien, N., 2001, “Large Strain Behaviour of Brain Tissue in Shear: Some Experimental Data and Differential Constitutive Model,” *Biorheology*, **28**(4), pp. 335–345.

[15] Hrapko, M., van Dommelen, J. A. W., Peters, G. W. M., and Wismans, J. S. H. M., 2006, “The Mechanical Behaviour of Brain Tissue: Large Strain Response and Constitutive Modelling,” *Biorheology*, **43**(5), pp. 623–636.

[16] Prevost, T. P., Balakrishnan, A., Suresh, S., and Socrate, S., 2011, “Biomechanics of Brain Tissue,” *Acta Biomater.*, **7**(1), pp. 83–95.

[17] Ogden, R. W., 1984, *Non-Linear Elastic Deformations*, Wiley, Chichester, UK.

[18] Spencer, A. J. M., 1984, “Constitutive Theory of Strongly Anisotropic Solids,” *Continuum Theory of the Mechanics of Fibre Reinforced Composites* (CISM Courses and Lectures), Vol. 282, A. J. M. Spencer, ed., Springer, Berlin, pp. 1–32.

[19] Okamoto, R. J., Feng, Y., Genin, G. M., and Bayly, P. V., 2013, “Anisotropic Behavior of White Matter in Shear and Implications for Transversely Isotropic Models,” *ASME Paper No. SBC2013-14039*.

[20] Feng, Y., Okamoto, R. J., Namani, R., Genin, G. M., and Bayly, P. V., 2013, “Measurements of Mechanical Anisotropy in Brain Tissue and Implications for Transversely Isotropic Material Models of White Matter,” *J. Mech. Behav. Biomed. Mater.*, **23**, pp. 117–132.

[21] Tenti, G., Sivaloganathan, S., and Drake, J. M., 1999, “Brain Biomechanics: Steady-State Consolidation Theory of Hydrocephalus,” *Can. Appl. Math. Q.*, **7**(1), pp. 111–124.

[22] Franceschini, G., Bigoni, D., Regitnig, P., and Holzapfel, G. A., 2006, “Brain Tissue Deforms Similarly to Filled Elastomers and Follows Consolidation Theory,” *J. Mech. Phys. Solids*, **54**(12), pp. 2592–2620.

[23] Mihai, L. A., Chin, L. K., Janmey, P. A., and Goriely, A., 2015, “A Hyperelastic Constitutive Model for Compression Stiffening Applicable to Brain and Fat Tissues,” *J. R. Soc. Interface*, **12**(110), p. 20150486.

[24] Ogden, R. W., 1972, “Large Deformation Isotropic Elasticity—On the Correlation of Theory and Experiment for Incompressible Rubberlike Solids,” *Proc. R. Soc. London A*, **326**(1567), pp. 565–584.

[25] Mooney, M., 1940, “A Theory of Large Elastic Deformation,” *J. Appl. Phys.*, **11**(9), pp. 582–592.

[26] Rivlin, R. S., 1948, “Large Elastic Deformations of Isotropic Materials. IV. Further Developments of the General Theory,” *Philos. Trans. R. Soc. London A*, **241**(835), pp. 379–397.

[27] Rivlin, R. S., and Saunders, D. W., 1951, “Large Elastic Deformations of Isotropic Materials. VII. Experiments on the Deformation of Rubber,” *Philos. Trans. R. Soc. London A*, **243**(865), pp. 251–288.

[28] Gent, A. N., 1996, “A New Constitutive Relation For Rubber,” *Rubber Chem. Technol.*, **69**(1), pp. 59–61.

[29] Holland, M. A., Miller, K. E., and Kuhl, E., 2015, “Emerging Brain Morphologies From Axonal Elongation,” *Ann. Biomed. Eng.*, **43**(7), pp. 1640–1653.

[30] Holzapfel, G. A., and Gasser, T. C., 2001, “A Viscoelastic Model for Fiber-Reinforced Composites at Finite Strains: Continuum Basis, Computational Aspects and Applications,” *Comput. Methods Appl. Mech. Eng.*, **190**(34), pp. 4379–4403.

[31] Gasser, T. C., Ogden, R. W., and Holzapfel, G. A., 2006, “Hyperelastic Modelling of Arterial Layers With Distributed Collagen Fibre Orientations,” *J. R. Soc. Interface*, **3**(6), pp. 15–35.

[32] Cloots, R. J. H., van Dommelen, J. A. W., Nyberg, T., Kleiven, S., and Geers, M. G. D., 2011, “Micromechanics of Diffuse Axonal Injury: Influence of Axonal Orientation and Anisotropy,” *Biomech. Model. Mechanobiol.*, **10**(3), pp. 413–422.

[33] Laksari, K., Shafieian, M., and Darvish, K., 2012, “Constitutive Model for Brain Tissue Under Finite Compression,” *J. Biomech.*, **45**(4), pp. 642–646.

[34] Simo, J. C., and Miehe, C., 1992, “Associative Coupled Thermoelasticity at Finite Strains: Formulation, Numerical Analysis and Implementation,” *Comput. Methods Appl. Mech. Eng.*, **98**(1), pp. 41–104.

- [35] Ommaya, A. K., 1968, "Mechanical Properties of Tissues of the Nervous System," *J. Biomech.*, **1**(2), pp. 127–136.
- [36] Galford, J. E., and McElhane, J. H., 1970, "A Viscoelastic Study of Scalp, Brain, and Dura," *J. Biomech.*, **3**(2), pp. 211–221.
- [37] Sack, I., Beierbach, B., Hamhaber, U., Klatt, D., and Braun, J., 2008, "Non-Invasive Measurement of Brain Viscoelasticity Using Magnetic Resonance Elastography," *NMR Biomed.*, **21**(3), pp. 265–271.
- [38] Kruse, S. A., Rose, G. H., Glaser, K. J., Manduca, A., Felmlee, J. P., Jack, C. R., Jr., and Ehman, R. L., 2008, "Magnetic Resonance Elastography of the Brain," *NeuroImage*, **39**(1), pp. 231–237.
- [39] Green, M. A., Bilston, L. E., and Sinkus, R., 2008, "In Vivo Brain Viscoelastic Properties Measured by Magnetic Resonance Elastography," *NMR Biomed.*, **21**(7), pp. 755–764.
- [40] Feng, Y., Clayton, E. H., Chang, Y., Okamoto, R. J., and Bayly, P. V., 2013, "Viscoelastic Properties of the Ferret Brain Measured In Vivo at Multiple Frequencies by Magnetic Resonance Elastography," *J. Biomech.*, **46**(5), pp. 863–870.
- [41] Sack, I., Beierbach, B., Wuerfel, J., Klatt, D., Hamhaber, U., Papazoglou, S., Martus, P., and Braun, J., 2009, "The Impact of Aging and Gender on Brain Viscoelasticity," *NeuroImage*, **46**(3), pp. 652–657.
- [42] Streitberger, K.-J., Sack, I., Krefling, D., Pfüller, C., Braun, J., Paul, F., and Wuerfel, J., 2012, "Brain Viscoelasticity Alteration in Chronic-Progressive Multiple Sclerosis," *PLoS One*, **7**(1), p. e29888.
- [43] Mendis, K. K., Stalnaker, R. L., and Advani, S. H., 1995, "A Constitutive Relationship for Large Deformation Finite Element Modeling of Brain Tissue," *ASME J. Biomech. Eng.*, **117**(3), pp. 279–285.
- [44] Miller, K., and Chinzei, K., 1997, "Constitutive Modelling of Brain Tissue: Experiment and Theory," *J. Biomech.*, **30**(11–12), pp. 1115–1121.
- [45] Miller, K., 1999, "Constitutive Model of Brain Tissue Suitable for Finite Element Analysis of Surgical Procedures," *J. Biomech.*, **32**(5), pp. 531–537.
- [46] Miller, K., Chinzei, K., Orsengo, G., and Bednarz, P., 2000, "Mechanical Properties of Brain Tissue In-Vivo: Experiment and Computer Simulation," *J. Biomech.*, **33**(11), pp. 1369–1376.
- [47] Miller, K., and Chinzei, K., 2002, "Mechanical Properties of Brain Tissue in Tension," *J. Biomech.*, **35**(4), pp. 483–490.
- [48] Prange, M. T., and Margulies, S. S., 2002, "Regional, Directional, and Age-Dependent Properties of the Brain Undergoing Large Deformation," *ASME J. Biomech. Eng.*, **124**(2), pp. 244–252.
- [49] Rashid, B., Destrade, M., and Gilchrist, M. D., 2013, "Mechanical Characterization of Brain Tissue in Simple Shear at Dynamic Strain Rates," *J. Mech. Behav. Biomed. Mater.*, **28**, pp. 71–85.
- [50] Li, K., Zhao, H., Liu, W., and Yin, Z., 2015, "Material Properties and Constitutive Modeling of Infant Porcine Cerebellum Tissue in Tension at High Strain Rate," *PLoS One*, **10**(4), p. e0123506.
- [51] Pamidi, M. R., and Advani, S. H., 1978, "Nonlinear Constitutive Relations for Human Brain Tissue," *ASME J. Biomech. Eng.*, **100**(1), pp. 44–48.
- [52] Budday, S., Raybaud, C., and Kuhl, E., 2014, "A Mechanical Model Predicts Morphological Abnormalities in the Developing Human Brain," *Sci. Rep.*, **4**, p. 5644.
- [53] Wagner, M. H., 1976, "Analysis of Time-Dependent Non-Linear Stress-Growth Data for Shear and Elongational Flow of a Low-Density Branched Polyethylene Melt," *Rheol. Acta*, **15**(2), pp. 136–142.
- [54] Phan-Thien, D. N., Safari-Ardi, M., and Morales-Patiño, A., 1997, "Oscillatory and Simple Shear Flows of a Flour-Water Dough: A Constitutive Model," *Rheol. Acta*, **36**(1), pp. 38–48.
- [55] Arruda, E. M., and Boyce, M. C., 1993, "A Three-Dimensional Constitutive Model for the Large Stretch Behavior of Rubber Elastic Materials," *J. Mech. Phys. Solids*, **41**(2), pp. 389–412.
- [56] Ahmadzadeh, H., Smith, D. H., and Shenoy, V. B., 2014, "Viscoelasticity of Tau Proteins Leads to Strain Rate-Dependent Breaking of Microtubules During Axonal Stretch Injury: Predictions From a Mathematical Model," *Biophys. J.*, **106**(5), pp. 1123–1133.
- [57] van den Bedem, H., and Kuhl, E., 2015, "Tau-ism: The Yin and Yang of the Microtubule Sliding, Detachment, and Rupture," *Biophys. J.*, **109**(11), pp. 2215–2217.
- [58] Hakim, S., Venegas, J. G., and Burton, J. D., 1976, "The Physics of the Cranial Cavity, Hydrocephalus and Normal Pressure Hydrocephalus: Mechanical Interpretation and Mathematical Model," *Surg. Neurol.*, **5**(3), pp. 187–210.
- [59] Miga, M. I., Paulsen, K. D., Hoopes, P. J., Kennedy, F. E., Hartov, A., and Roberts, D. W., 2000, "in vivo Modeling of Interstitial Pressure in the Brain Under Surgical Load Using Finite Elements," *ASME J. Biomech. Eng.*, **122**(4), pp. 354–363.
- [60] Shahim, K., Drezet, J. M., Martin, B. A., and Momjian, S., 2012, "Ventricle Equilibrium Position in Healthy and Normal Pressure Hydrocephalus Brains Using an Analytical Model," *ASME J. Biomech. Eng.*, **134**(4), p. 041007.
- [61] Drapaca, C. S., and Fritz, J. S., 2012, "A Mechano-Electrochemical Model of Brain Neuromechanics: Application to Normal Pressure Hydrocephalus," *Int. J. Numer. Anal. Model.*, **3**(1), pp. 82–93.
- [62] García, J. J., and Smith, J. H., 2008, "A Biphase Hyperelastic Model for the Analysis of Fluid and Mass Transport in Brain Tissue," *Ann. Biomed. Eng.*, **37**(2), pp. 375–386.
- [63] Støverud, K. H., Darcis, M., Helmig, R., and Hassanizadeh, S. M., 2011, "Modeling Concentration Distribution and Deformation During Convection-Enhanced Drug Delivery Into Brain Tissue," *Transp. Porous Media*, **92**(1), pp. 119–143.
- [64] Biot, M. A., 1941, "General Theory of Three-Dimensional Consolidation," *J. Appl. Phys.*, **12**(2), pp. 155–164.
- [65] Kaczmarek, M., Subramaniam, R. P., and Neff, S. R., 1997, "The Hydromechanics of Hydrocephalus: Steady-State Solutions for Cylindrical Geometry," *Bull. Math. Biol.*, **59**(2), pp. 295–323.
- [66] Lang, G. E., Vella, D., Waters, S. L., and Goriely, A., 2015, "Propagation of Damage in Brain Tissue: Coupling the Mechanics of Oedema and Oxygen Delivery," *Biomech. Model. Mechanobiol.*, **14**(6), pp. 1197–1216.
- [67] Bayly, P. V., Taber, L. A., and Kroenke, C. D., 2014, "Mechanical Forces in Cerebral Cortical Folding: A Review of Measurements and Models," *J. Mech. Behav. Biomed. Mater.*, **29**, pp. 568–581.
- [68] Kaliske, M., and Rother, H., 1997, "Formulation and Implementation of Three-Dimensional Viscoelasticity at Small and Finite Strains," *Comput. Mech.*, **19**(3), pp. 228–239.
- [69] Budday, S., Nay, R., de Rooij, R., Steinmann, P., Wyrobek, T., Ovaert, T. C., and Kuhl, E., 2015, "Mechanical Properties of Gray and White Matter Brain Tissue by Indentation," *J. Mech. Behav. Biomed. Mater.*, **46**, pp. 318–330.
- [70] Brands, D. W. A., Peters, G. W. M., and Bovendeerd, P. H. M., 2004, "Design and Numerical Implementation of a 3-D Non-Linear Viscoelastic Constitutive Model for Brain Tissue During Impact," *J. Biomech.*, **37**(1), pp. 127–134.
- [71] Lee, E. H., 1969, "Elastic-Plastic Deformation at Finite Strains," *ASME J. Appl. Mech.*, **36**(1), pp. 1–6.
- [72] Sidoroff, F., 1974, "Un Modèle Viscoélastique Non Linéaire Avec Configuration Intermediaire," *J. Mec.*, **13**, pp. 679–713.
- [73] Rodriguez, E. K., Hoger, A., and McCulloch, A. D., 1994, "Stress-Dependent Finite Growth in Soft Elastic Tissues," *J. Biomech.*, **27**(4), pp. 455–467.
- [74] Nedjar, B., 2002, "Frameworks for Finite Strain Viscoelastic-Plasticity Based on Multiplicative Decompositions. Part I: Continuum Formulations," *Comput. Methods Appl. Mech. Eng.*, **191**(15–16), pp. 1541–1562.
- [75] Reese, S., and Govindjee, S., 1998, "A Theory of Finite Viscoelasticity and Numerical Aspects," *Int. J. Solids Struct.*, **35**(26–27), pp. 3455–3482.
- [76] Sadowski, T. J., 1965, "Non-Newtonian Flow Through Porous Media—II: Experimental," *Trans. Soc. Rheol. (1957–1977)*, **9**(2), pp. 251–271.
- [77] Larson, R. G., and Brenner, H., 1988, *Constitutive Equations for Polymer Melts and Solutions*, Butterworth-Heinemann, Boston, MA.
- [78] Bergström, J. S., and Boyce, M. C., 2001, "Constitutive Modeling of the Time-Dependent and Cyclic Loading of Elastomers and Application to Soft Biological Tissues," *Mech. Mater.*, **33**(9), pp. 523–530.
- [79] Diani, J., Fayolle, B., and Gilormini, P., 2009, "A Review on the Mullins Effect," *Eur. Polym. J.*, **45**(3), pp. 601–612.
- [80] Mullins, L., 1969, "Softening of Rubber by Deformation," *Rubber Chem. Technol.*, **42**(1), pp. 339–362.
- [81] Chagnon, G., Veron, E., Gornet, L., Marckmann, G., and Charrier, P., 2004, "On the Relevance of Continuum Damage Mechanics as Applied to the Mullins Effect in Elastomers," *J. Mech. Phys. Solids*, **52**(7), pp. 1627–1650.
- [82] Simo, J. C., 1987, "On a Fully Three-Dimensional Finite-Strain Viscoelastic Damage Model: Formulation and Computational Aspects," *Comput. Methods Appl. Mech. Eng.*, **60**(2), pp. 153–173.
- [83] Dorfmann, A., and Ogden, R. W., 2004, "A Constitutive Model for the Mullins Effect With Permanent Set in Particle-Reinforced Rubber," *Int. J. Solids Struct.*, **41**(7), pp. 1855–1878.
- [84] El Sayed, T., Mota, A., Fraternali, F., and Ortiz, M., 2008, "A Variational Constitutive Model for Soft Biological Tissues," *J. Biomech.*, **41**(7), pp. 1458–1466.
- [85] Taylor, D. W., 1948, *Fundamentals of Soil Mechanics*, Wiley, New York.
- [86] Koeneman, J. B., 1966, "Viscoelastic Properties of Brain Tissue," M.S. thesis, Case Institute of Technology, Cleveland, OH.
- [87] Christ, A. F., Franze, K., Gautier, H., Moshayedi, P., Fawcett, J., Franklin, R. J. M., Karadottir, R. T., and Guck, J., 2010, "Mechanical Difference Between White and Gray Matter in the Rat Cerebellum Measured by Scanning Force Microscopy," *J. Biomech.*, **43**(15), pp. 2986–2992.
- [88] Gefen, A., and Margulies, S. S., 2004, "Are In Vivo and In Situ Brain Tissues Mechanically Similar?" *J. Biomech.*, **37**(9), pp. 1339–1352.
- [89] Zhang, J., Green, M. A., Sinkus, R., and Bilston, L. E., 2011, "Viscoelastic Properties of Human Cerebellum Using Magnetic Resonance Elastography," *J. Biomech.*, **44**(10), pp. 1909–1913.
- [90] Genet, M., Lee, L. C., Baillargeon, B., Guccione, J. M., and Kuhl, E., 2016, "Modeling Pathologies of Systolic and Diastolic Heart Failure," *Ann. Biomed. Eng.*, **44**(1), pp. 112–127.
- [91] Budday, S., Steinmann, P., and Kuhl, E., 2014, "The Role of Mechanics During Brain Development," *J. Mech. Phys. Solids*, **72**, pp. 75–92.
- [92] Budday, S., Steinmann, P., and Kuhl, E., 2015, "Physical Biology of Human Brain Development," *Front. Cell. Neurosci.*, **9**, pp. 257.1–257.17.
- [93] Budday, S., Kuhl, E., and Hutchinson, J. W., 2015, "Period-Doubling and Period-Tripling in Growing Bilayered Systems," *Philos. Mag.*, **95**(28–30), pp. 3208–3224.
- [94] Songbai, J., Ghadyani, H., Bolander, R., Beckwith, J. G., Ford, J. C., McAllister, T. W., Flashman, L. A., Paulsen, K. D., Ernstrom, K., Jain, S., Raman, R., Zhang, L., and Greenwald, R. M., 2014, "Parametric Comparisons of Inter-Cranial Mechanical Responses From Three Validated Finite Element Models for the Human Head," *Ann. Biomed. Eng.*, **42**(1), pp. 11–24.
- [95] Mazumder, M. M. G., Miller, K., Bunt, S., Mostayed, A., Joldes, G., Day, R., Hart, R., and Wittek, A., 2013, "Mechanical Properties of the Brain-Skull Interface," *Acta Bioeng. Biomech.*, **15**(2), pp. 3–11.
- [96] Bayly, P. V., Clayton, E. H., and Genin, G. M., 2012, "Quantitative Imaging Methods for the Development and Validation of Brain Biomechanics Models," *Annu. Rev. Biomed. Eng.*, **14**(1), pp. 369–396.